Processing-Structure-Performance Relationships in Fused Filament Fabricated Fiber Reinforced ABS for Material Qualification

William H. Ferrell, PhD
Stephanie TerMaath, PhD

This research was conducted under Naval Education Engineering Consortium grant N00174-16-C0033, under the direction of Dr. Maureen Foley at the Naval Surface Warfare Center Carderock Division.

Abstract

Fused filament fabrication (FFF) is an additive manufacturing technique that utilizes the layering of deposited molten plastic to create three dimensional objects. This technique has gained traction over the past two decades as a disruptive manufacturing technology that promises many benefits. For widespread acceptance of FFF in manufacturing spaces across the world for the production of end-user parts, standardization of testing procedures for the qualification of FFF specific materials are required. A better understanding of the process-microstructure-performance relationships is essential to achieve this goal. This research aimed to characterize some of these relationships (specifically the effects of print parameters on tensile and interface fracture behavior) to provide results and conclusions to inform the development of qualification standards for FFF parts.

In Section 1, a comprehensive analysis of the current state of the art in fracture of FFF parts is presented and discussed. The rheological specific phenomena that govern the polymer chain physics at interfaces and within deposited beads is included due to its impact on the mechanical properties of the printed material. In Section 2, a commonly used tensile testing standard is explored and demonstrated on carbon fiber reinforced acrylonitrile-butadiene-styrene (ABS). Due to the complex manufacturing process, new naming standards and testing recommendations are made and the influence of part production methodologies and processing parameters on ultimate tensile strength are explored. The response of fiber reinforced and non-reinforced ABS in environmental conditioning is tested and discussed in Section 3. Specimens were exposed to heat and moisture to represent onboard conditions and evaluated under tension loading. Section 4 introduces a potential testing specimen for obtaining multiple fracture modes. Through this test specimen, the nature of the material as a laminate or as a porous homogeneous material is explored.

Table of Contents

1 Fracture behavior of fused filament fabricated polymers: A Review

1.1 Abstract

Despite rapid progress throughout the past few decades, standardization of fused filament fabrication (FFF) techniques and comprehensive characterization of the end-use material behavior remains essential for the FFF manufacture of reliable parts for use as primary structure. Due to the complex nature of the FFF process, strength and stiffness-based material qualification processes alone are not adequate to ensure structural reliability considering the complex rheology, microstructure, and macrostructure of FFF parts. Emphasis on developing a deeper understanding of the processing-structure-performance relationships, effects of defects, and fracture mechanics is essential to fully realize the potential of FFF in the manufacturing landscape. This review consolidates these relevant topics from polymer chain physics to material and part characterization as it pertains to the fracture behavior of FFF products with the goals of informing future work and generating a repository of current knowledge.

1.2 Introduction

Fused filament fabrication (FFF) is popular worldwide in industry use and makerspaces due to its low cost, availability,[1] and ease for manufacturing specialized on-demand or customized parts.[2] Through the heating, extrusion, and layered deposition of thermoplastic material, a three dimensional object is produced that relies on the mechanical crosslinking of the polymer chains between beads of material for strength. In the preceding decades, characterization of FFF parts and materials has been performed through numerous studies investigating air voids,[3-5] additives such as fibers and nanocomposites,[6-15] the chemical makeup,[16][17] and the overall mesostructure of the print and part itself.[18-21] Introducing a filler, such as carbon fiber,[9][22-31] glass fiber,[32] or organic materials,[10][33] can result in improved material properties in FFF parts, and as such, reinforced material is readily available. FFF provides scalability of the manufacture of small parts, such as plastic caps produced using desktop printers,[34] to much larger structures, such as a submarine printed through Big Area Additive Manufacturing (BAAM),[35] allowing for this technique to span a wide range of potential applications.

A necessity for the widespread implementation of FFF parts is the development of material qualification standards to ensure structural reliability. Due to the complex nature of standards development and the rapid development in FFF, most research efforts have focused on utilizing

numerous ASTM International and International Organization for Standardization (ISO) testing standards to correlate additives, microstructure, chemical makeup, etc. to the strength and stiffness of those materials.[36-41] Other factors, such as material response under environmental conditions [42-44], that influence part performance have also been investigated to quantify their detrimental effects on strength. When discussing the scope of effort necessary to qualify materials for end-use, fracture mechanics becomes ever more important in FFF parts due to the manufacturing process itself.[45-47] As the nozzle deposits molten material in a set raster pattern, many potential crack initiation sites are formed including voids, defects, and areas of weak adhesion. Therefore, fracture analysis plays an essential role in the prediction of FFF part failure.

There are three dominant regions for fracture to occur in FFF parts: through the bead (intrabead), between layers (interlayer), and between beads in a given layer (interbead), **Figure 1**, creating a complex environment for crack initiation and growth. For example, the size and shape of the voids between beads (**Figure 2**) are dependent on the raster pattern (path of bead deposition) and can be a site of crack initiation, cause multiple crack coalescence, or propagate a single crack through the void. Interlayer and interbead domains where the contact area is smaller or where the polymer chains have poor interdiffusion can initiate and propagate delamination between beads. And, additives or imperfections in the material can create voids and defects in the beads prompting cracks to grow intrabead. As seen in **Figure 2**, cracks in FFF parts commonly propagate through varying domains, necessitating the need for multiple fracture mechanics principles to define and predict crack growth. When a crack grows interlayer or interbead, the interlaminar fracture toughness standards used in the composites industry are applicable, however if a crack grows completely intrabead, fracture toughness standards for homogeneous material matrices or chopped fiber composites are needed. It is important to note that the current composite standards should be updated to reflect FFF attributes. A primary goal of this review is to provide a consolidated source of the state-of-the-art in fracture characterization and testing to inform the development of testing standards specific to FFF.

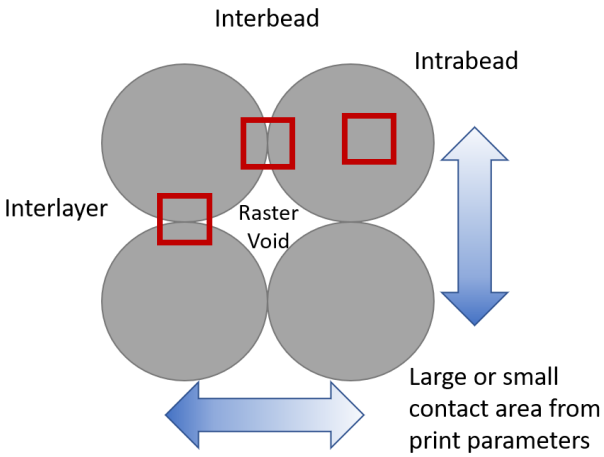

Figure 1. Layer and bead overlap is dictated by the printing parameters and affects the three major fracture domains boxed in red

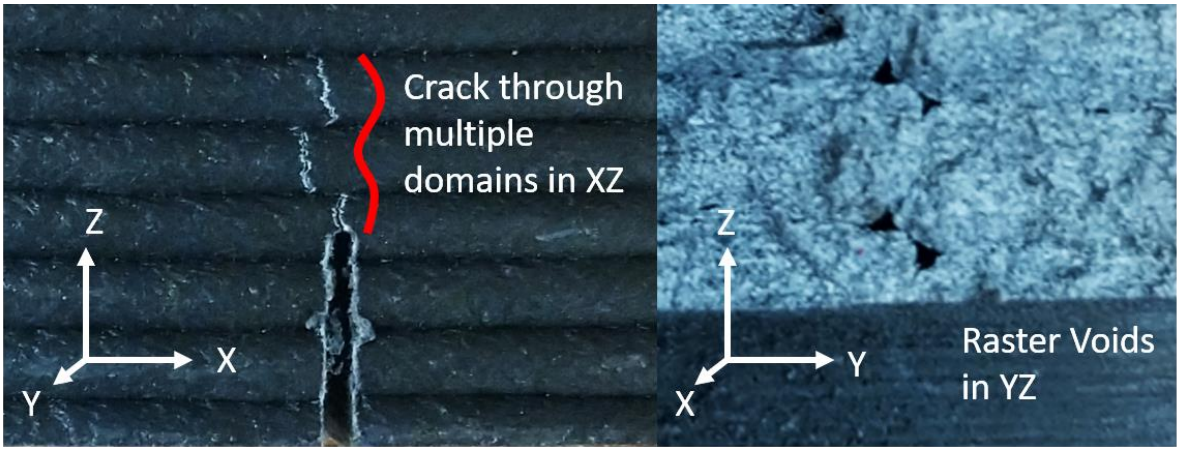

Figure 2. Crack deviations caused by raster voids, weak interdiffusion, and internal defects imparted by the manufacturing process dictated by the polymer chain dynamics in FFF

With creation of FFF specific fracture testing standards in mind, the processing-structure-performance relationships require continued investigation to expand our knowledge of this critical correlation that directly influences fracture behavior. Fabrication based on the user-specified printing parameters creates cascading effects starting with the part structure itself through the mechanical properties and the material behavior in the various fracture domains. As an example, higher printing temperatures have been shown to improve the interlayer adhesion, however, may simultaneously increase the intrabead void content.[48] Also, printing parameters that lead to poor layer adhesion, such as low printing temperatures, high fan speeds, etc, can cause cracks to grow in the interlayer region.[49] However, optimized printing conditions, which are later discussed, have been proven to create a homogeneous or near homogeneous matrix where the FFF part shows little dependency on the layer and bead adhesions.[45]

The printing parameter effects on fracture illuminate the rheological importance of polymer chain behavior in the melt during deposition. Research by Pascual-González et. al. demonstrates how the consistent use of dynamic mechanical analysis (DMA), thermogravimetric analysis (TGA), and DSC to analyze the factors behind the micromechanical response of FFF parts is important to the testing of FFF parts.[50] This work related the rheological and structural properties in the polymer matrices to strength and stiffness, however it has not been extended to fracture. FFF specific fracture testing standards and qualification procedures need to be developed that account for the multiple fracture domains as well as the complexities of the processing-structure-performance relationships in the FFF parts.

Through an exploration of the rheological phenomena and fracture mechanics concepts as applicable to FFF, a holistic compilation of the state-of-the-art knowledge on the fracture characterization of parts manufactured by FFF is reviewed. Discussion of topics spanning nano and micro-scale polymer chain physics through large scale FFF part production is presented in four sections: Phenomenological Complexity, Fracture and FFF, Small Scale versus Large Scale Fracture Behavior, and Big Area Additive Manufacturing (BAAM) FFF Fracture. Each topic provides a brief history of the scientific advancements, assumptions, and limitations of the state-of-the-art in fracture characterization of FFF parts. The objectives of this section are to guide future standard development of FFF material testing, to inform future research on fracture characterization, and to provide a consolidated review of current knowledge.

1.3 Phenomenological Complexity

Thermoplastic polymers are commonly used in FFF, because at elevated temperatures they behave as a fluid allowing for extrusion and then undergo a transition through the rubbery plateau during cooling to a glassy, or solid, state after deposition. An important effect of the extrusion and deposition process on the fracture behavior of the final part is the interdiffusion and amount of contact area between beads, as interfaces are a known source of FFF part failure.[25][48] Control of the printing process to ensure favorable conditions for mechanical crosslinking at interfaces as well as maximizing infill to reduce the number and size of voids improves fracture performance. The branch of physics that addresses this flow and deformation of matter is rheology, and this section discusses the effects of the printing process on the specific rheological phenomena[51–67] which govern the fracture behavior of the polymer used as the primary print material.

During the FFF deposition process, the molten polymer bead being deposited contributes heat to the adjacent bead and beads of the previous layer, that have already begun cooling, creating the necessary environment at the interfaces between the beads for layer mixing. As previously defined in **Figure 1**, the two types of interfaces are interlayer and interbead, and previous research has quantified differences in the behaviors of these two interfaces due to the variation in thermal conditions during the deposition process.[1] Melt viscosity and chain mobility, which are controlled by the print processing conditions, govern the overall mechanical crosslinking that provides the physical strength and fracture toughness, the materials resistance to crack propagation, of an interface. The melt viscosity determines the overall contact area between deposited beads, and the chain mobility determines the short range and long range interdiffusion. Polymers are held together by a combination of Van der Waals forces and covalent bonds, and for a crack to grow in a polymer matrix both must be overcome and broken. Because a crack propagates along the path(s) of least resistance, **Figure 3**, the contact area and polymer interdiffusion play a significant role in the crack behavior, where raster voids cause crack initiation and deviations and poor interdiffusion reduces the material's resistance to load.

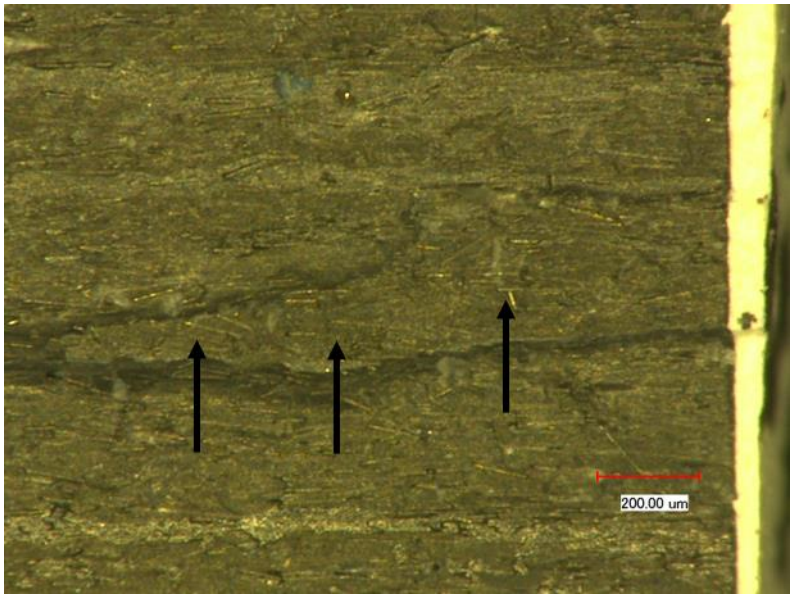

Figure 3. Crack propagated to the bead above the crack plane, specified by the arrows, as it followed the path of least resistance.

1.3.1 Tube Theory

It is well established that polymer processing during FFF induces various levels of stress, strains, and strain rates on the polymer chains within the material system.[40] Subsequently, the molecular structure of polymers plays an important role in the material response to various print parameters, such as print speed, extrusion temperature, and print bed temperature. The bulk material property of the printed polymer within the bead, or the intrabead properties, most likely mimic those of non-refeprinted polymers.[68] If confirmed by future research, mechanical properties of a printed bead could be obtained from testing on pre-printed filament with standard values provided by the manufacturer. This relationship would eliminate the need for considering and quantifying the effects of the nearly unlimited combinations of user specified print parameters on printed intrabead properties. The interfaces on the other hand vary substantially based on the print parameters.[69] During material deposition, a major constraint on the mechanical crosslinking, which dictates the interface strength and fracture toughness, may occur according to the tube concept. The tube concept originated from the inability of two polymer chains to cut through each other in the course of motion, thus dictating a tube-like region that confines each polymer chain. As shown in **Figure 4**, a single bead encompasses many thousands of tubes dictated by the molecular weight of the polymer and the polymer structure. Each region severely restricts the motion of chains orthogonal

to the tube and the tube contour.[70,71] The tube diameter is dependent on polymer chain properties such as monomer bulkiness and chain stiffness but not as much on chain length.[62] Thus different polymers will have different inherent monomer bulkiness and chain stiffness which in turn affects the entanglement size (N_e) and the statistical segment length (b) where the tube diameter (a) is equal to $N_e^{1/2}$*b. With fracture toughness dependent on the entanglements in the polymer matrix, the polymer chain mobility in the melt dictates the matrix formation at the interfaces in FFF. Because polymer chain mobility depends on the polymer chain properties, the printing parameters, such as speed and temperature, would not have uniform effects across all polymer types used in FFF. Therefore, the relationship between polymer chain mobility and mechanical properties must be uniquely considered for each polymer type.

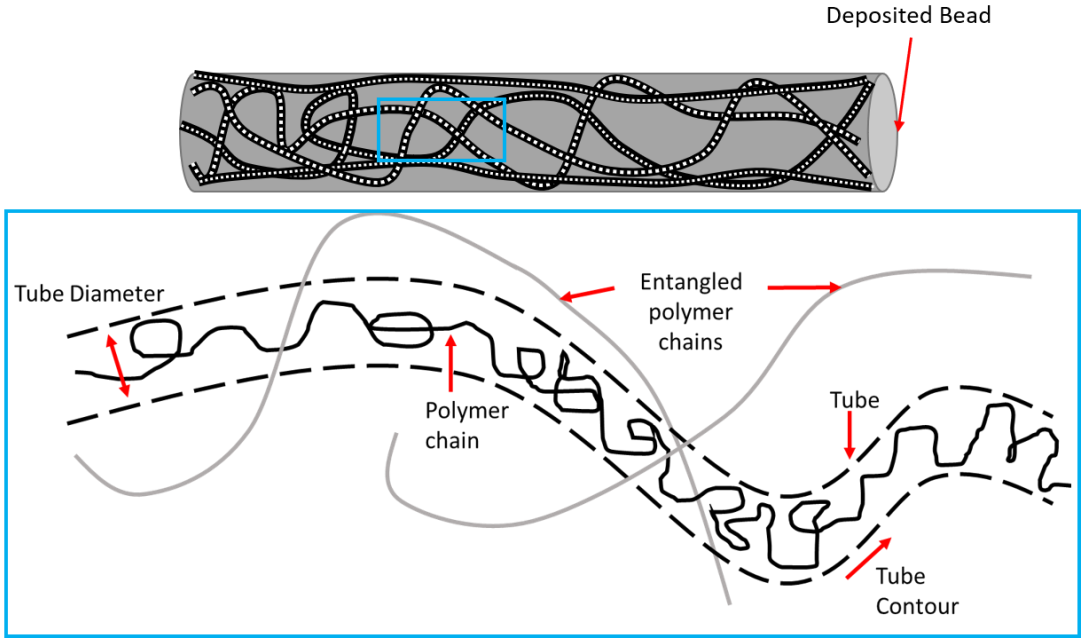

Figure 4. Representation of polymer chains within a deposited FFF bead and the associated tube that confines the polymer chains

For example, in the case of acrylonitrile-butadiene-styrene (ABS) versus polylactic acid (PLA), two of the most common FFF polymers, the constituent monomers are vastly different in size and mobility. For reference, polystyrene is one of the most common industrial polymers with applications in consumer durable goods, packaging, structural foams, lenses, cable sheathing, etc due to the ease of fabrication and low cost. When copolymerized with acrylonitrile to form styrene-acrylonitrile (SAN) there is an increase in the tensile strength, where the polarity in the acrylonitrile group creates a stronger matrix than pure polystyrene. In the case of ABS, **Figure 5**, the interspersed butadiene provides toughness to the strong SAN matrix due to butadiene's rubbery nature. Each of these structures have different sizes and shapes which impact the tube diameter, where the polystyrene suffers from steric hindrance, or restricted rotation, due to the size of the benzene rings and thus is the limiting factor in the ABS chain mobility. Compare this with the structure of PLA, **Figure 5**, where there are no bulky pendant groups in the lactic acid monomer or the lactide monomer, where condensation reactions are used to polymerize the lactic acid monomer and lactide is polymerized through ring-opening polymerization. Once again, much like in the butadiene, the side chain bonding and structure provides a more mobile polymer chain in the melt than the styrene in polystyrene or ABS. Each of these FFF plastics have vastly different tube sizes, in part from the polymer chain structure, that dictate the motion of the polymer chains in the melt. Because of the layering of molten plastic in FFF, a new polymer matrix is formed at the interfaces of each bead and layer, which highlights the importance of better understanding the governing polymer chain physics. Due to distinct polymer chain behavior for each print material, standardizing print parameters across all polymers may not be possible and instead must be optimized for each polymer type.

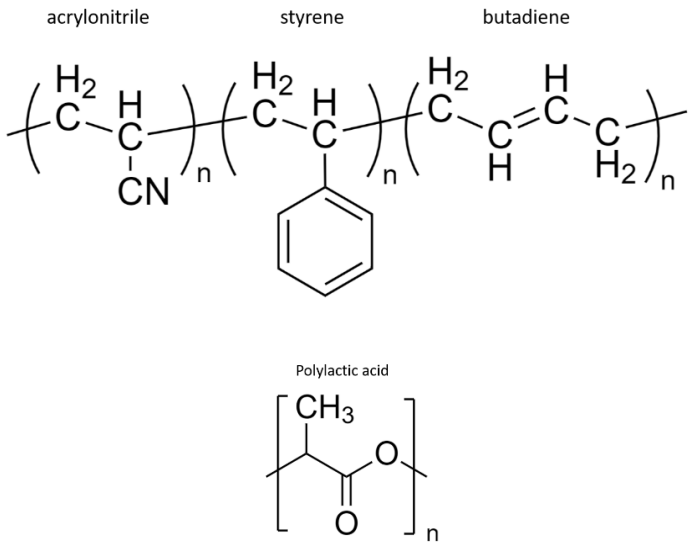

Figure 5. ABS polymer structure (top) where side chain size and type impact the overall polymer behavior and PLA polymer structure (bottom)

Due to the reliance of fracture toughness on the entanglement density of polymer chains and that the entanglement density is predicated on both the tube diameter and the polymer chain dynamics, better connection of polymer physics to mechanical behavior within FFF printed material is needed. Tube diameter is experimentally obtained by the comparison of measured rheological behavior to the predictions of theoretical models, which requires well entangled polymers on time scales shorter than the stress relaxation time for the polymer chains. Mathematically, several ansatzes, which are initial estimates and assumptions of the solution to a mathematical problem, are available to describe the tube diameter and entanglement behaviors in a number of ways. The most successful of such has been the Lin-Noolandi ansatz, which has had consistent success in describing experimental results for tube diameter in a wide range of polymers.[72–75] The Lin-Noolandi ansatz reveals how N_e varies with local chain dimensions, where bulkier monomers with a corresponding larger monomer volume, or more flexible chains with a smaller segment length increase the entanglement length. Equations 1 and 2 demonstrate the assertions of the Lin-Noolandi ansatz, where the number of chain segments cohabiting a volume pervaded by an entanglement strand is a universal constant for flexible polymers.[75]

$$\frac{\left(N_e^{\frac{1}{2}}b\right)^3}{N_e\Omega} = C \qquad \text{Eq 1.}$$

$$N_e = \frac{C^2\Omega^2}{b^6} \quad \text{Eq 2.}$$

Where $N_e^{1/2}b$ is the size of one entanglement strand, Ω is the monomer volume, and C is the universal constant roughly equal to 22.4.[75] Rephrasing these cases by replacing the entanglement size with the tube diameter, the packing length can be related to the monomer volume and the segment length. This packing length is the length which delineates the overfilling of space. By replacing N_e with $a = N_e^{1/2}b$ to obtain $a = C\,\Omega/b^2$ the packing length $p \equiv \Omega/b^2$. The associated size scale of local encounters between neighboring chain segments is the best description of the packing length. If an entanglement chain is not flexible enough or has bulky monomers, the inability to adopt compact random walk configurations inhibits other chain segments from approaching, necessary for entanglements. Thus, in the Lin-Noolandi ansatz, the tube diameter is proportional to the packing length.[74]

A second ansatz was proposed by Milner,[75] and Rubinstein and Colby in the study of polymer solutions in order to encapsulate the polymer chain behavior observed in said polymer solutions.[76] This ansatz asserts that the volume pervaded by one entanglement strand a^3 contains a constant number of close contacts between chain segments (C^3) and has a characteristic volume of a close contact equal to p^3. A third ansatz was recently introduced by Qin et. al. in the study of oriented and stretched polymer melts, indicative of melts in strong aligning flows. This ansatz asserts a fixed number of close contacts between an entanglement strand and neighboring chains.[62] And, even in highly concentrated polymer solutions, the polymer chain behaviors, including the nonlinear viscoelastic properties, differ from that of polymer melts.[77,78] The difference in polymer chain behavior in solution and in the melt are seen in the difference in prediction for how the tube diameter changes when comparing ansatz II and ansatz III. As pertaining to FFF and fracture, inhibition of the entanglement chains greatly reduces the fracture toughness of the interface between beads and layers. To better understand polymer entanglements in the melt, mathematical ansatz III most closely relates the boundary conditions of the printing process with polymer entanglement. Print speed, print temperature, polymer type, fan speed, and bed temperature all play a part in the polymer chain dynamics in orienting and stretching flow.

1.3.2 Polymer Melts in FFF conditions

Due to the environment of oriented and stretched polymer melts, created by the FFF process, further discussion of the Qin and Milner ansatz, ansatz III, is discussed in regards to the conceptualizing of polymer entanglements in oriented and stretched polymer melts at the interlayer and interbead interfaces.[62]As the polymer melt is deposited onto the previous layer, the polymer chains are stretched at various intensities depending on the print speed. Higher print speed results in larger shear forces that stretch and orient the polymer chains, **Figure 6**. The effects of this stretching and orienting is discussed, but first, a better understanding of polymer chain level behavior must be established.

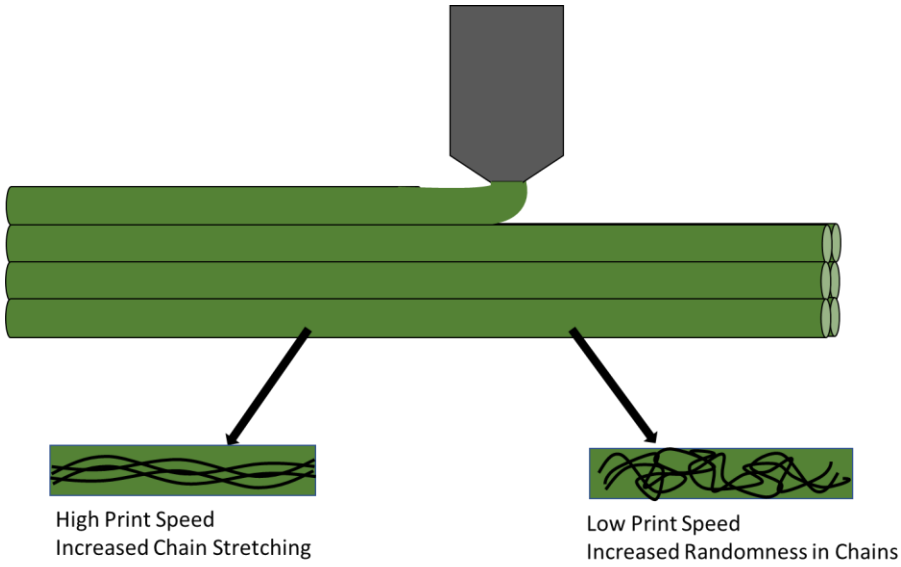

Figure 6. Print speed dictates the chain conformation and can lead to a more oriented or less oriented chain structure.

In the deposition process of FFF and the subsequent restriction of the motion of the polymer chains in a polymer melt once deposited, the tension applied to a bead creates changes in the molecular motion itself. Polymer chains are commonly modeled as random walks, where the location or movement of the end of the polymer chain moves as a stochastic process. The force extension in the system is most likely not large enough to fully extend the polymer chains and thus be affected by the limit of full extension, where a fully extended chain is restricted in motion. Thus, the polymer chains can be described rheologically by Gaussian random walks, which is the stochastic process based on step sizes that vary according to a normal distribution. This Gaussian random

walk can then be used to determine the configuration free energy of a Gaussian chain under uniaxial pulling.[62] The configuration free energy can be written as:

$$\frac{3kTR^2}{2Nb^2} - FR_z \qquad \text{Eq 3.}$$

Where k is Boltzmann's constant, T is temperature, R is the end to end separation vector, N is entanglement size, b the statistical segment length, F is force, and R_z is the end to end separation vector along the length of the tube. From this relationship, Qin and Milner demonstrated a force dependence and a crossover tube diameter analysis that is reliant on how close the chains achieve maximum elongation. For isotropic melts, the pervaded volume is estimated as a^3, but for chains under tension it is estimated using the volume of the cylinder pervaded by a test strand.[62] The extension of ansatz III to a fixed number of contacts per entanglement strand when deformed to an isotropic melt at fixed topological complexity predicts a scaling of tube diameter so long as the force is not large enough to bring the chains to full extension. This application of ansatz III provides consistent results with experimental data without large adjustments of N_l away from the Kuhn length.[62] Qualitatively, ansatz III asserts that the chains stretched out along a direction have a lesser tendency to fill the space around their own monomers and subsequently have more room for entanglement strands from nearby chains and additional contacts. This stretching has a twofold effect on the potential strength and fracture toughness of the part.

The first effect is the increase in the overall number of contacts between polymer chains, which as discussed previously, increases the space available for polymer entanglements. Increased entanglements result in the increased mechanical crosslinking that helps provide the materials resistance to fracture. However, the second effect is in direct opposition to the first, where the increased stretch of the polymer chains also causes a decrease in the tube diameter discussed above. As applied to FFF, for a constant volume of extruded material, increasing the print speed is associated with a decreased melt viscosity of the material, shear thinning, caused by the disentanglement of polymer chains. When sheared, polymer chains begin to disentangle and align which causes the observed viscosity to drop, and the degree of disentanglement is shear rate dependent. While this orienting can create more potential contacts for entanglements between polymer chains, the overall contact area is decreased between the deposited beads and large voids are manufactured into the part.

Qualitatively in ansatz III, there is a decrease in both the tube diameter and N_e for chains under tension, where there is a lesser tendency of polymers to fill the space around their own monomers. This relationship is also consistent with a binary view of entanglements as binary interactions between chains, which are the result of chain-shrinking algorithms.[79,80] This binary view is also supported by simulation results on primitive path rearrangements that occur as a result of two chain segments crossing over each other in the melt.[81] The topological entropy can be interpreted in such a way as to having these chains approach, interact, and either wrap around or not, then so on and so forth. This environment creates the random dodging and interacting necessary to produce the randomly braided structure that is the entangled polymer melt. However, with the rapid cooling in the FFF system, there are changes to the boundary conditions allowing for the interactions necessary for those randomly braided structures.

Thermodynamically, each system seeks to maximize entropy, through the reduction of order, and polymer chain entanglements are the result, however when energy is introduced to the system in the form of shear stress, the resulting topological entropy is changed. The orienting of chains creates an environment for short range interdiffusion, where these shallower interactions dominate in the structure. In order to achieve the highest resistance to fracture, a heavier reliance on the covalent bonds of the polymer chains is needed. This means that the ends of polymer chains need to be able to diffuse across layers and deep within adjacent beads. This long-range diffusion is stifled by the orienting and stretching of polymer chains, **Figure 6**. In terms of impact on fracture, this creates a layer-to layer and bead-to-bead contact area with high reliance on the weaker Van der Waals forces that can be more easily deformed and yield at the crack tip, seen as crazing. Pairing this condition with increased void content could potentially lead to a macroscopic brittle behavior, despite the microscopic conditions that contribute to ductile fracture.

Leveraging the polymer rheology of stretched chains in the melt provides the possibility of tailoring areas in a part for a specific property using print parameters and opens up interesting future avenues in predictive computational modeling. In the case of tensile testing performed by Ferrell et. al.[69] there was a phenomenon noticed where higher printing temperatures, which provide better diffusion and theoretically higher strength, led to a slightly lower ultimate tensile strength and a much higher elongation to break with load applied only to the interface between beads. Ultimately as this finding pertains to fracture and future tailoring of parts, the pairing of

low print speeds and high nozzle temperature could create areas of higher toughness, and simultaneously pairing standard nozzle temperature and higher print speeds could create areas of higher strength. Future molecular dynamics simulations for the predictions of polymer chain locations with FFF boundary conditions and structural dynamics simulations for testing crack growth in FFF materials can eliminate this conjecture.

1.3.3 Polymer Diffusion for Bead Contacts

Polymer diffusion, which is the primary mechanism in which the FFF deposited beads interact with previous beads, is an additional area that demonstrates the impact of entanglements, temperature, and molecular weight.[82] The Doi-Edwards theory has a direct relation with diffusion and temperature.[83] Recent work has investigated and elaborated on polymer architectures effect on polymer dynamics in the melt[84] due to the Rouse model not being generally applicable even in the simple case of unentangled polymers.[85,86] When discussing polymer diffusion and the computations surrounding it, hydrodynamic radius (R_h) and radius of gyration (R_g) are introduced, and while they are more commonly reserved for polymer solutions, they do appear in polymer melt texts, which could extend to future FFF investigations. These terms are defined as the average distance of a chain element from the center of gravity of the chain and are proportional for a linear chain molecule.[55] These values are required when calculating the diffusion coefficient D.

The interpretation of the diffusion work and scaling laws as it relates D to R_h and R_g is that, in a coarse grain sense, polymer chains are comparable to tracer particles which "sense" local viscosity differences form the macroscopic viscosity. Diffusion is then predicated on the sizing of those particles and as such the radius size of the particles, when compared to the R_h and R_g, must be similar for this hypothesis to hold, which it does according to the data collected by Chremos et. al.[84] The hypothesis of particles in diffusion comparing to the R_h and R_g extends to rationalizing the dependence of D based on the hydrodynamic polymer size by conceptualizing polymers in the melt as soft particles. The conceptual relationship of polymers in the melt as soft particles can then be extended to entangled polymer systems by assumption of a transition similar to that found in the Stokes-Einstein relation. This transition is observed in dynamically heterogeneous liquids due to the formation of particles clusters, and if such a transition exists on the scale of R_g to heterogeneous polymer dynamics underlying the entanglement phenomenon, then the power law

scaling transition of shear viscosity would occur.[84] Chremos et. al. suggest that the transition between the power law scaling observed for all different polymer architectures can be rationalized as the emergent dynamical heterogeneity that is characteristic of strongly interacting soft particle systems.[87]

It is of note that higher printing temperatures or printing parameters that allow the print to stay hotter longer can counteract the stretching and orienting effects discussed earlier. By keeping the system at a higher temperature, the capacity for the polymer chains to reach more entropically favorable configurations is increased which presents itself as a reduction of the internal stresses imparted by the manufacturing process. The increased capability of the polymer chains to reach more favorable configurations is the concept behind annealing systems, but because the FFF process constantly is adding heat to the system with each deposited layer, an annealing type reaction is expected in the previous layers, depending on how long the polymer chains remain above a temperature that allows high chain mobility. The extent to which the polymer chains can move and anneal is discussed above and is tied to the hydrodynamic radius or the radius of gyration of the polymer chains in question. It is also dictated by whether the polymer can form crystalline domains in which the crystalline versus amorphous domains are impacted by the temperature. The more favorable the entropic conformations, as shown in **Figure 7**, of the polymer chains at the interface are, the more resistant that interface is to crack growth.

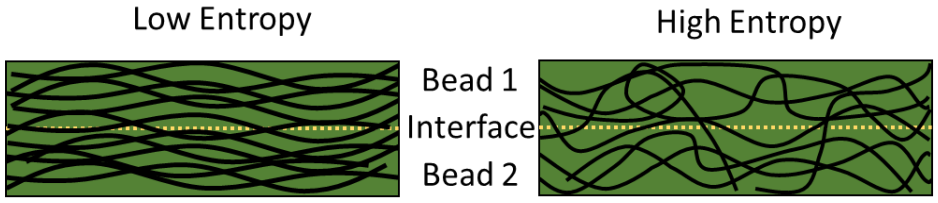

Figure 7. The lower entropy system on the left relies on fewer polymer chains to resist fracture at the interface due to a lack of long-range diffusion

Keeping the previously discussed annealing in mind, Song. et. al. demonstrated that in a PLA system, the FFF process led to a higher percent crystallinity as compared to the injection molding using differential scanning calorimetry (DSC).[88] This was then associated with an increase in the fracture toughness of the material. However, when the researchers annealed the FFF test specimens, they found no increase in the percent crystallinity but found a decrease in the overall

strength. Through the annealing process of PLA, it is expected that there would be an increase in the crystalline domain size or number of crystalline domains, increasing the overall percent crystallinity. The stretching and orienting effect of the polymer during deposition could be the limiting factor for increased crystallinity, where the chains reached a certain topological entropy that was limited. If the highest crystallinity was achieved, the crystalline regions impeded the polymer chains in the amorphous phase during the annealing process. The polymer chain mobility restriction hypothesized by the crystalline domains is an interpretation of the potential causes by the authors and was not further investigated by Song et. al., but that hypothesis does demonstrate an increased need in the research of FFF specific phenomena at the polymer chain level during the FFF process.

1.3.4 Rheological Phenomena: Slip Springs and Beyond

The modeling and understanding of polymer chain dynamics is ever evolving without a consensus on the molecular basis of polymer rheology itself. Much like the aspirations in other branches of physics, a reductionist truth of fundamental polymer physics has been pursued since the theories introduced by Kuhn, Flory, and de Gennes.[89–91] Advances in the experimental measurement and technology surrounding polymer physics has seen coinciding advances in the rheological theory, and thus it is likely that FFF could provide further testing grounds for modeling and testing. Due to the complex boundary conditions of changing temperature, pressure, orientations, etc, further development of the molecular dynamics simulations of polymer chains provide an interesting proving ground for better understanding polymer chain dynamics.

A competing model to the tube theory[92] and evidence of contradictory behavior of polymer chains under extension[78] are provided by several more recent advancements in polymer rheology that are of importance for future predictive modeling of FFF. One of the competing models for polymer chain dynamics was developed by Likhtman et al that contests the future value of the tube theory due to a lack of definition of the primitive path in terms of chain coordinates.[64,93] This contestation has led to the above discussion on tube theory where certain explanations and ansatz do not hold in different environments such as melts versus solutions. The primary parameter in tube theory is the singular number of entanglements, but if tube theory is not a single parameter theory, then finding this number of entanglements is not pertinent.[64] Likhtman et. al. proposed the slip-spring model which states individual entanglements can

potentially be modeled by slip-springs and subsequently defines entanglements as persistent contacts between the mean paths of polymer chains.[64] The slip-springs concept suggests that tube diameter, *a*, does not impact the fluctuations of the chain perpendicular to the tube, but only the properties along the contour. The impact of the tube dimeter only affecting the properties along the contour changes the physical meanings of the parameters *a* and N_e, or Z as listed in the referenced work. Instead, a constructed freely jointed chain with a certain contour length and average square end-to-end distance would have Z steps of length *a* in an equivalent chain. The change of the physical meaning of the parameters *a* and Z separates the number of entanglements from the associated mathematical parameter by changing the interpretation.

Further work exploring the slip-spring model includes expansion into contour length fluctuations and constraint release.[94–96] An important take away from these works is the ability to model various constraint release environments and slow chain versus fast chain behavior. In the case of FFF where the part has varying heat transfer into the system after initial deposition, the overall ability to more readily track and predict chain locations in multiple different constraining environments is important. One of the major advantages of the slip spring model for researchers is the contribution of a model with the equations of motion for chain coordinates clearly specified which is lacking in the aforementioned tube theories. In the expansion and exploration of the constraint release and contour fluctuations, there is preliminary success of applying a tube model description to the results of a slip-spring model. This agreement provides some evidence that these two different approaches can be reconciled and unified in the future.

On a fundamental level, in FFF literature, the reptation of polymer chains between layers dictates the mechanical crosslinking necessary to provide the toughness of the manufactured part. The governing concepts explored above in relation to polymer chain behavior and entanglements still hold, but it is important to note that the way in which we model the behavior of polymer chains can increase the change in how those materials resist fracture, and therefore their calculated fracture toughness. Changes in how polymer entanglements are viewed and therefore modeled need to be included in the adaption of fracture mechanics for FFF. While utilizing the governing rheology and thermodynamics to conceptualize changes in fracture toughness is one aspect, the predictive modeling and integrated computational materials engineering worlds require accurate polymer chain and rheology models.

1.4 Fracture Mechanics and FFF

Before World War II, there was little emphasis placed on material defect or crack propagation in a material. It was thought that these small cracks could not affect the grand structures built of steel during this time. However, after a series of catastrophic failures in the 1940s-1950s, including the hull cracking of the SS Schenectady and the three fatal de Havilland Comet crashes, rapid expansion in the field of fracture mechanics occurred.[97,98] Fracture mechanics is the encompassing field in solid mechanics that addresses the propagation of a crack through the material and the material's ability to resist this failure. During this same time, the damage tolerance approach to engineering design gained traction due to the emphasis it placed on a material's ability to withstand a small enough amount of damage that could be detected during inspection and be repaired prior to failure through a maintenance plan, to design and build safer structures. At the heart of this damage tolerance approach is the ability to predict crack growth through a material using fracture mechanics principles. Given the complexity of modern engineered parts, such as those fabricated with FFF, the need for advanced fracture mechanics testing, modeling, and analysis has never been greater. This section discusses the current state-of-the-art and future needs in fracture mechanics for FFF.

1.4.1 Fracture Mechanics Concepts and Terminology

In order to better understand the current state of the art in fracture specific to FFF, a brief history and discussion with regards to the different fracture terminology and concepts is provided. Previously discussed intrabead, interbead, and interlayer regions, **Figure 1**, within an FFF part all have different rheological concerns as outlined above, but also create the need for different fracture terminology and tests to be applied. The establishment of fracture mechanics was based on observations by A. A. Griffith[99] when analyzing the failure of bulk glass, where the stress needed to break bulk glass was about 100x less than the stress needed to break the atomic bonds of glass. To reconcile this difference, Griffith hypothesized the presence of microscopic flaws in the bulk material. To test this hypothesis, Griffith introduced a large surface crack in the material and found that the stress to cause fracture multiplied by the square root of the crack size was almost constant. This finding however, created a conundrum in linear elastic materials where the stress at the tip of a sharp flaw is infinite. A thermodynamic approach was subsequently introduced to explain this relation. As a crack propagates the surface areas on either side of the crack grow, therefore increasing the surface energy. This correlation allowed the stress at fracture (σ_f) of a specified

crack length (a) to be related to the Young's modulus of a material (E) and the surface energy density of the material (γ).

$$\sigma_f \sqrt{a} = \sqrt{\frac{2E\gamma}{\pi}} \quad \text{Eq 4}$$

$$\sigma_f \sqrt{a} = \sqrt{\frac{EG_c}{\pi}} \quad \text{Eq 5}$$

The quantity 2γ was combined into the Griffith Critical Energy Release Rate, G_c, directly relating the force of fracture to the bond energy. As the applicability of Griffith's finding was limited to brittle material systems, additional investigation under the direction of G. R. Irwin at the Naval Research Laboratory advanced its relevance to a much larger range of materials which would include metals and then later polymers.

Despite the applicability Griffith's equation to steel, the predicted surface energy was unrealistically high for ductile materials. Irwin et. al. theorized the role of plasticity at the crack tip in affecting the fracture of ductile materials, which includes the polymer material systems currently used in FFF.[100] In a ductile material, a plastic zone forms in front of the crack tip and grows with increasing stress until the crack propagates and the elastically strained material behind the crack tip is unloaded. Due to a cyclic plastic loading at the crack tip, energy is dissipated in the form of heat and Irwin subsequently introduced a dissipative term, G_p. Depending on the brittle or ductile nature of the material meant that the surface energy density (γ) or the dissipative term (G_p) respectively dominated in the energy release rate, G, as shown in Rquation 6.

$$G = 2\gamma + G_p \quad \text{Eq 6}$$

Irwin and his colleagues next introduced the ability to calculate the amount of energy needed for fracture based on the asymptotic stress and displacements around the crack tip in a linear elastic solid, Equation 7 where σ_{ij} are the Cauchy stresses, r is the distance from the crack tip, θ is the angle with respect to the plane of the crack and f_{ij} are functions dependent on geometry. The stress field around the crack was related to the value K, the stress intensity factor. Beyond the stress field relationship, he proposed that if the plastic zone is small compared to the size of the crack, a purely

elastic solution may be used to calculate the energy needed for fracture using K. The stress intensity factor relationship to the energy release rate is shown in Equation 8.

$$\sigma_{ij} = \frac{K_I}{\sqrt{2\pi r}} f_{ij}(\theta) \quad \text{Eq 7}$$

$$G = G_I = \begin{cases} \frac{K_I^2}{E} & plane\ stress \\ \frac{(1-\nu^2)K_I^2}{E} & plane\ strain \end{cases} \quad \text{Eq 8}$$

When G reaches the critical value, G_c, fracture becomes unstable. The corresponding critical value of K is called fracture toughness denoted as K_{Ic} in the plane strain condition for mode I. There are three different modes in fracture mechanics depending on the loading system. Mode I is characterized as crack opening, mode II as in plane-sliding, and mode III as out of plane tearing. Very commonly a material will experience some mixed-mode type loading requiring the determination of mixed mode fracture properties. Fracture properties may be dependent on material orientation. For example, within crystalline polymeric systems used in FFF, grain boundaries and orientations caused naturally or by the manufacturing process can cause orientation specific material intrabead properties.

In order for a material system to be treated as a linear elastic problem, the fracture must be brittle, but many polymeric systems undergo too much yielding and must be analyzed using elastic plastic fracture mechanics. Both Rice[101] and Cherepanov[102] independently developed a new toughness measure in the case where sufficient deformation at the crack tip occurs. Both showed that an energetic contour integral around the crack was path independent and was named as the J-integral. The J_{Ic} is the mode I strain energy release rate per unit fracture area for elastic-plastic fracture mechanics (EPFM) and in the J-integral approach, it reduces to the Griffith criteria for linear-elastic fracture mechanics (LEFM).

While the above concepts apply to intrabead fracture, additional consideration is needed for interface damage prediction, because the interfaces between layers appear to have different properties than the bead material. Within FFF parts there are many interfaces between beads that behave similarly to the interfaces between lamina in composite laminates. For example, in the case of a composite laminate, interlaminar fracture toughness testing is used to quantify delamination between the lamina. The distinction is made between fracture tests of homogeneous materials and

composite materials in the current ASTM and ISO standards[103], and both types of tests are needed to characterize fracture in FFF parts.

1.4.2 Linear Elastic Fracture Mechanics for FFF

Several studies on FFF fracture toughness have been performed using the LEFM framework laid by Griffith and Irwin. Song et. al.[88] produced three sets of single edge notch bend (SENB) test specimens, machining these specimens from 0° and 90° FFF polylactic acid (PLA) blocks, **Figure 8**, as well as an injection-molded PLA block. The SENB test specimen is a standard test for plane-strain fracture toughness of plastic materials.[104] The 0° specimen was designed to test the intrabead fracture toughness and the 90° specimen was designed to test the interlayer fracture toughness. The test set up employed a laser extensometer and a digital image correlation (DIC) system to observe the displacement as these tests. Song et. al. produced an R-curve for the fracture toughness from the test results, where the stress intensity factor K is plotted as a function of the crack extension. The results demonstrate that the FFF material is tougher than that of the injection molded material and the fracture toughness is higher in the 0° direction when compared to the 90° print direction.

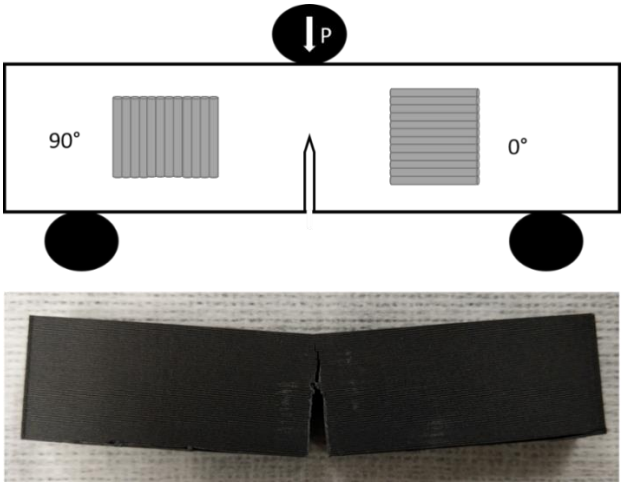

Figure 8. SENB specimen with the two bead orientations and an example printed SENB specimen post testing with varied crack path due to printing orientation

These results are explained because the ultimate tensile strength in the 0° print direction is higher than that of the 90° print direction, but the higher fracture toughness of the 90° print direction compared to that of the injection molded PLA is unexplained. The 90° print direction specifies

loading directly onto the layer and bead interfaces which from tensile testing has shown to have weaker adhesion leading to the explanation of orientation dependence. However, a fully homogeneous part from the molded specimen should theoretically have superior toughness. The authors concluded that there were very different methods of crack propagation at play due to the filamentous nature of the FFF part. For the 0° specimen, the crack advanced in a single plane with an occasional kink by 90° causing delamination between the inter-layers, resulting in dissipation of additional energy. For the 90° specimen, the crack advanced in an irregular fashion where the topology of the fracture surface possessed a higher surface area characterized by a wavy fracture surface. The fracture surface of the injection molded specimen was much smoother than those of the FFF printed parts. This fracture surface suggested a surface boundary layer with different mechanical properties that were consequential with the non-uniform cooling rates in the injection molding process.

Song et. al. concluded that the mechanical response of FFF PLA was anisotropic and asymmetric in nature with a direction-dependent fracture behavior.[88] Also compared to the homogeneous injection molded PLA, the FFF specimens had a higher crystallinity, reducing the ductility of the material and increasing the fracture toughness. This increased toughness is due to the layered and filamentous nature of the 3D printed material and the associated complexity induced in the microscopic mechanisms of fracture.

McLouth et. al. further investigated intrabead fracture by correlating fracture toughness (K_{Ic}) variation with mesostructure in FFF parts through the use of compact tension tests.[105] The compact tension (CT) specimens for mode I fracture toughness tests used in this study were printed in multiple orientations containing various raster orientations. The print orientations were labelled XZY, XYZ, and ZXY with XY defining in-plane directions and Z the out-of-plane direction. Therefore, the material is deposited in the XY plane and then built up with layers in the Z direction. So, these specimens were printed on the bed in three different configurations with two different patterns for the infill of the part. This notation is important to define the orthotropic nature of the parts, but also provides a point of confusion in comparing studies due to varying terminology and experimental controls. With the XZY print orientation, the crack was planar to the XY plane and the two raster orientations were 0°/90° and +45°/-45°. In the XYZ print orientation, the crack was planar to the XZ plane and were printed with the same two raster orientations as the XZY. Finally,

the ZXY print was printed with the crack planar to the ZY plane, also with the same raster orientations.

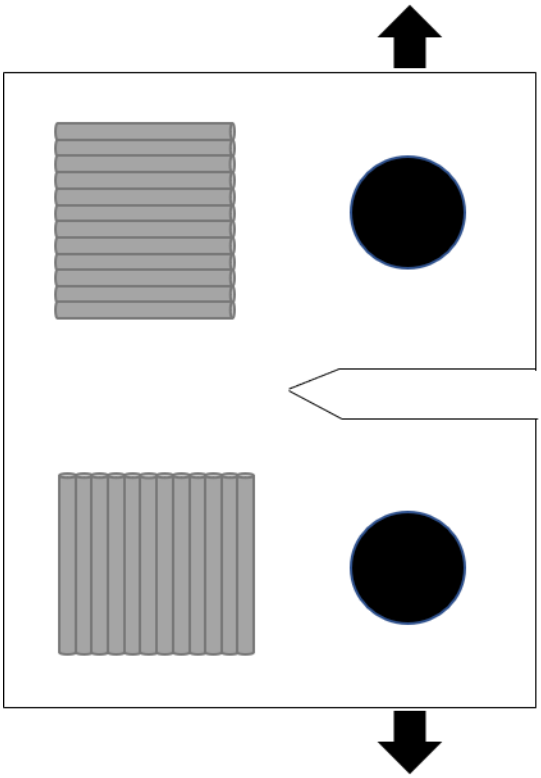

Figure 9. CT test specimen with two potential orientations to measure fracture between layers (top) and through the bead (bottom).

McLouth et. al. found that the print and raster orientation in the CT samples significantly impacted the fracture toughness. [105] It is noted that in the work by McLouth et. al. they found that the specimens exceeded the conditions needed to be reported as true linear-elastic plane-strain fracture toughness requirements. In the two orientations that had half or more of their filaments orthogonal to the crack plane, the fracture toughness was higher due to these filaments being an obstacle to crack propagation. These fracture toughness values were in the middle of reported ranges for bulk ABS with the range of K_{Ic} being roughly 1.1-4 MPa*$m^{1/2}$. In the other orientation the fracture toughness was lower due to a reliance on the weak interfilament bonding. The toughness, as reported in

Table 2, was on the lower side of the reported toughness values for bulk ABS. It was also reported that when filaments adjacent to the crack tip were loaded along their axis, the plastic zone was larger. The plastic zone size dependence provides a compelling argument of the importance of the mesostructure to the measured fracture toughness in FFF. Additionally, in the +45°/-45° specimens the mesostructure encouraged branching which showed improve toughness, however this deviation to a mixed mode of failure contributes to increased energy dissipation and increased toughness. Mesostructural effects are an important analysis when discussing the qualification of material versus certification of parts, where the material resistance to fracture is impacted heavily by the mesostructure and therefore becomes even more application dependent.

1.4.3 Elastic-Plastic Fracture Mechanics in FFF

Previous work in the strength and stiffness domains have endeavored to determine fully optimized printing parameters for FFF polymers such as PLA. The goal of these studies was to determine how to fabricate an FFF part without producing a substantial number of voids in the final part due to the raster pattern. A study performed by Arbeiter et. al. examined the fracture properties of PLA produced by FFF in the CT and SENB test configurations for orientations of 0°, 90°, and 0°/90° printed using optimized parameters[45], and several important observations were made. One observation was that for monotonic loading, the LEFM criteria could not be met, therefore the EPFM criteria or the J-integral should be used for fully optimized printing conditions. For these tests the J integral was evaluated according to the following two equations based on the SENB standard[106]:

$$J_0 = \frac{\eta U}{B(W-a_0)} \quad \text{Eq 9}$$

$$J = J_0 * \left(1 - \frac{(0.75\eta-1)\Delta a}{W-a_0}\right) \quad \text{Eq 10}$$

where, U is the integral of the force-displacement (P-δ) curve, η is a geometry dependent factor, a_0 is the initial crack length, and Δa is the incremental crack propagation.[106] Both W and B are geometry values from the test specimen of length and width respectively. This study was performed with the three-point bend test using the SENB test specimen to determine mode I fracture toughness.

The results from this study demonstrated that there were no voids or other processing induced defects for the 0° and 90° specimens, but some small observable defects were seen in the 0°/90° specimen. The 90° specimen had the highest fracture toughness with the 0° and 0°/90° specimens comparable. Upon inspection, Arbeiter et. al. found that there was slightly more area of plastically deformed material, shear lips and ruptured fibrils, on the fracture surface compared to the other orientations.[45] The slight improvement of ductility could be explained by the shorter time between bead depositions in this orientation. Arbeiter et. al. note that for the 0° orientation the beads are deposited over the length of 44 mm, where they were only printed over a length of 10 mm for the 90° specimen. Due to the insulating nature of polymeric material, the high cooling rates of the surface of each deposited bead compared to the middle could be a reason for the difference in fracture toughness and observed ductility. Arbeiter et. al. recommended further exploration using more sophisticated morphology characterizations such as small angle x-ray scattering (SAXS) or wide-angle x-ray scattering (WAXS) to provide further insight into the morphology and fracture-mechanical properties. This recommendation by Arbeiter et. al. further supports the need for advanced rheological experimentation to pair with the FFF specific processes to elucidate the processing-structure-performance relationships.

1.4.4 Interlaminar Fracture in FFF

Hart et al performed the same SENB test previously mentioned on ABS polymer and described the printed specimens as “laminates”, where each lamina is a layer of material parallel to the print bed with a nominal thickness of the corresponding layer height.[107] Specimens were then designed to examine the orthotropic fracture behavior of this ABS material, where vertically printed SENB samples, horizontally printed SENB samples, and obliquely printed SENB samples were manufactured to encompass the various orientations. The vertically printed SENB specimens were designed to test the inter-laminar fracture toughness, the horizontally oriented SENB samples were designed to test the cross-laminar fracture toughness, and the obliquely oriented SENB samples provided qualitative results corresponding to fracture between and across laminae.

In the vertically printed SENB specimens, Hart et al found that the mode I stress intensity factor K_{Ic} and the critical elastic-plastic strain energy release rate J_{Ic} were comparable to brittle solids and not typical of plastically deformable polymers like bulk ABS. The observed brittle fracture was contradicted by the evidence of tearing-type fracture at the interface which is common for

ductile materials. However, regions of un-fractured material were observed as a result of the porosity and individual raster lines were also identifiable. As compared to the Song et al study, the processing parameters of the specimens in this study were not optimized to maximize infill and minimize porosity. Hart et al hypothesized that the fracture behavior in the specimens is strongly influenced by magnitude and regularity of the porosity; where areas of high weld line overlap cause stress to build up and as crack initiation ensues, the crack moves to the fracture plane of least resistance which corresponds to regions of high porosity. In the case of these vertically printed SENB specimens, it is noted in the literature that there is a reduced ultimate tensile strength that is heavily influenced by layer time and build height on small scale printers.[69]

In the case of the horizontally oriented SENB specimens, multiple types of fracture are observed through SEM micrographs. A Power law fit was employed in the J-R curve and deviations were attributed to the high variability in FFF parts, which is well documented.[69] There was significant whitening in the crack propagation region as a result of crazing, indicative of elastic-plastic deformation. Crazing occurs in polymers due to the materials combination of weak Van der Waals forces and strong covalent bonds. For tension loading conditions, local stress overcomes the Van der Waals forces and results in a small crack but it is not enough to break the covalent bonds. This crazing happens in front of the crack front before crack propagation in these testing configurations. Within the SEM micrographs of the crack propagation region, porosity attributed to the manufacturing process is visible, as well as micro-porosity in the material. This micro-porosity was attributed to the cavitation process during failure provided by the butadiene component.

The measured cross-laminar elastic-plastic J_{Ic} is comparable to that of injection molded ABS SENB specimens but are slightly lower. This slightly lower value was attributed to the porosity present in the FFF process. Higher porosity decreases the overall material volume and results in increased crack propagation. Interestingly enough in this study, laminae orientation dictated the crack path based on the obliquely oriented tests, and crack path did in fact follow the weaker fracture toughness, the inter-laminar toughness. Hart. et. al found that the interlaminar fracture toughness was almost an order of magnitude lower than that of the cross-laminar fracture.

Aliheidari et. al. employed the double cantilever beam (DCB) test specimen in order to test the fracture resistance and interlayer adhesion of FFF printed ABS, **Figure 10**, due to the nature of the layered structure and the considerable impact the adhesion between layers has on the mechanical

properties.[108] This standard specifies testing for the mode I interlaminar fracture toughness of unidirectional fiber reinforced composites. The DCB test specimen was chosen due to the prevalence of beam-type fracture specimens for fracture characterization of layered materials. This test specimen was printed to the specified dimensions directly onto the bed with all the layers oriented in the longitudinal direction, **Figure 10**. This control of the print direction in this case results in the same interface and print conditions locally in sequential layers where cross hatched layers would have provided additional variability.

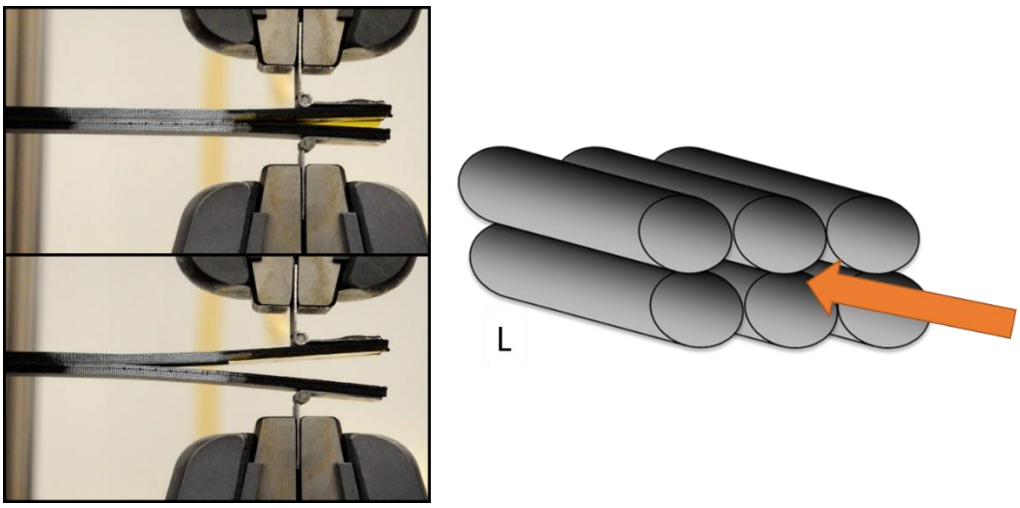

Figure 10 Example of DCB test specimen loaded in tension for mode I fracture toughness shown on left. Shown on the right is the orientation of the beads longitudinally with the orange arrow showing crack direction.

In the results of this testing the load increased, but at a nonlinear decreasing rate, after crack initiation started and before the onset of an unstable, sudden crack growth. The load increase was attributed to the toughening or the damage zone development ahead of the crack tip. An increase in the load before crack initiation was observed for specimens with a higher nozzle temperature, which is attributed to the better layer adhesion in higher print temperature parts. Additionally, the amount of surface intact was greatly increased with increasing nozzle temperatures. The surface intact ratio specified by Aliheidari et al is the ratio of the actual and nominal fracture surface areas. So, in this case due to the voids imparted by the FFF process, there is not a uniform and completely homogeneous cross section. The higher surface intact ratio is attributed to the viscosity of the

polymer melt at different temperatures affecting the surface area contact, as discussed in the previous sections.

The apparent fracture resistances of these specimens, measured using the J-integral method, significantly increased with increased print temperature. The resistance to fracture is a coupled consequence of the interlayer adhesion and the mesostructural features. Aliheidari et. al. decoupled these two by introducing the interlayer fracture resistance calculated by the surface intact ratio. It is noteworthy that even when adjusting for the mesostructural effects, the interlayer J_{Ic} did not converge to a single value, indicating a stronger mechanical crosslinking present in higher print temperatures. These values were comparable to bulk ABS when printed at 240°C and agrees with the dynamics discussed in previous sections, where increased temperature and increased time at temperature allow for a greater inter-diffusion of polymer chains between layers.

Interlayer fracture toughness was also investigated by Young et. al. using a modified version of the ASTM D5528 DCB specimen.[46] These specimens were compared to the same ABS and carbon fiber reinforced ABS (CF-ABS) material manufactured using hot press molding (HPM) and in the SENB configuration. Young et. al. found a reduction in the fracture toughness compared to the HPM specimens and that the fracture toughness of the CF-ABS was lower than the unreinforced ABS in both cases. In the case of the DCB tests, both materials demonstrated some nonlinearity prior to macroscopic crack extension, likely due to crack tip plasticity or onset of the crack at the center of the specimen. The amount of fracture toughness reduction imparted by the FFF process of two-fold for ABS and ten-fold for CF-ABS, resulting from the ductile and brittle fracture respectively. The explanation was that the CF-ABS rasters cool much quicker, reaching the glass transition temperature four times quicker than pure ABS. This rapid reduction in temperature results in decreased ability for the polymer chains to reptate between layers. Young et. al. note that the processing parameters were not optimized for fracture toughness and instead were optimized to produce a reproducible test. This distinction is currently an important component of FFF research, where mesostructured versus material properties are hard to discern and often times compound effects.

In the work done by Spoerk et. al. however, the interlayer strength in PLA was evaluated parametrically by analyzing the various effects of layer height and deposition temperatures on two different raster patterns of printed PLA specimens.[109] The interlayer fracture toughness was

evaluated using the DCB specimen and the two patterns consisted of layers stacked directly on top of each other and shifted to an extent to where the beads sat on top of the contact area between the beads in the previous layer, **Figure 11**.

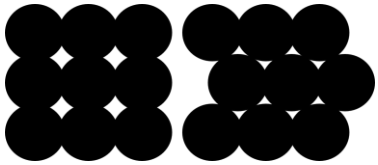

Figure 11. Two different stacking patterns used to investigate the interlayer adhesion.

Spoerk et. al. found that the shifted layer-design outperformed the stacked layer design for intra-layer loadings, however the stacked layer design provided the best fracture toughness for interlayer loading.[109] They also reported that higher printing temperatures create more plastic deformation during testing and in the highest printing temperature, craze formations and irregular crack paths were observed similar to those that a molded part would exhibit. When the printing parameters were optimized for inter-layer strength, Spoerk et. al. found parts with homogeneous cross-sections, high degrees of diffusion between layers and the aforementioned failure surfaces. They concluded that under the best settings, the DCB test, which is meant to test layered structures, did not provide any insight into the inter-layer cohesion and suggest that under optimal printing conditions, other tests such as the SENB test be used.

1.4.5 Complexity of fracture in FFF

Fracture mechanics as a field is a century old and considerable progress has been made encompassing various material systems, elastic-plastic behavior, inclusions, voids, and other complex behaviors relevant to the damage tolerance of FFF parts. The advancements in fracture mechanics have created a wealth of knowledge but also demonstrate the importance of choosing the appropriate test type for the material and fracture behavior under consideration. Additionally, relating microscopic phenomena to macroscopic response to load is a cornerstone of fracture mechanics and with that comes the need for further evaluation of FFF relative to the material microstructure which is governed in large part by the print parameter settings.

A major observation by Arbeiter et. al. was that the fracture behavior is not highly dependent on the printing orientation when the print parameters are optimized.[45] Arbeiter et. al. found that the

90° orientation demonstrated higher ductility which was attributed to less time between subsequent rasters and therefore good thermodynamic conditions for interdiffusion and crystalline domain formation. The orientation independent behavior was only observed in the SENB specimens and Arbeiter et. al. attributed that to the specimen shape and symmetry differences between the CT and SENB specimens. This study shows that it is possible to achieve almost homogeneous fracture toughness in FFF test specimens.

The change in the fracture toughness to be independent of orientation suggests that the internal mesostructure is itself a toughening mechanism that can be explored. The two prominent domains are the interlayer and the intrabead with a relatively brittle interlayer and the tougher intrabead. These two domains interact within a part that is printed with multiple directions causing potential toughening through mixed mode fracture.[105] However much like in other polymer based materials there was an increase of toughness with fiber content to a point. Each system and additive creates variance where the returns diminish, but it is common that additives such as fibers can create initiation sites for further crack propagation within the matrix.[110] Increasing the fiber content increases the elastic moduli and adds in voids causing a move towards more brittle fracture. Overall the major contribution to the toughness in the FFF polymer system is the covalent bonding of the polymer chains and the overall mixing obtained, where the near homogeneous fracture surface demonstrated equal or higher fracture toughness in mode I. With the complex nature of the FFF parts in mind, a summary of available data for the fracture toughness of FFF plastics is provided in **Tables 1, 2, and 3**.

Table 1. Test specimen and fracture toughness of PLA by various authors to date with standard deviation (S.D.) provided when available. Not valid designates specimens that exceeded the linear elastic range and therefore K or G do not apply.

PLA

	Test Specimen	Orientation	K_{Ic} (MPa $m^{1/2}$)	S.D.
Song et. al [88]	SENB	0°	5.05	0.19
		90°	4.06	0.15
		moulded	2.87	0.51

PLA

	Test Specimen	Orientation	K_{Ic} (MPa $m^{1/2}$)	S.D.	J_{Ic} (J/m^2)	S.D.
Arbeiter et. Al [45]	CT	0°	Not valid	-	-	-
		90°	Not valid	-	-	-
		0°/90°	Not valid	-	-	-
	SENB	0°	-	-	5750	-
		90°	-	-	6790	-
		0°/90°	-	-	5960	-

PLA

	Test Specimen	Top	G_{Ic} (J/m^2)	S.D.
Spoerk et. al.[109]	DCB	220°C /0.3mm	3850	340
		200°C/0.25mm	1300	200
		250°C/0.25mm	Not valid	high
		210°C/0.25	5100	690
		210°C/0.2	2000	600
		Shifted		
		220°C/0.3mm	1180	150

Table 2. Test specimen and fracture toughness of ABS and CF-ABS by various authors to date with standard deviation (S.D.) provided when available.

ABS

	Test Specimen	Orientation	K_{Ic} (MPa $m^{1/2}$)	S.D.	J_{Ic} (J/m^2)	S.D.
Hart et. al.[110]	SENB	0°	-	-	2260	-
		90°	0.789	0.131	256	84
		75°	-	-	-	-
	SENB from Lu et. al	moulded	-	-	3600-5900	-

			ABS		CF-ABS	
	Test Specimen	**Print Condition**	**G_{Ic} (J/m^2)**	**S.D.**	**G_{Ic} (J/m^2)**	**S.D.**
Young et. al.[46]	DCB	225°C	1800	210	360	60
			G_{Ic} (J/m^2)	**S.D.**	**G_{Ic} (J/m^2)**	**S.D.**
	SENB	hot press moulded	3440	150	3090	380

			ABS			
	Test Specimen	**Nozzle Temperature**	**J_{Ic} (J/m^2) apparent**	**S.D.**	**J_{Ic} (J/m^2) corrected**	**S.D.**
Aliheidari et. al[108]	DCB	210°C	953.71	29.83	2167.56	67.62
		230°C	21720	60.77	3560.65	99.62
		240°C	2731.87	119.94	3907.55	143.13

Table 3. Test specimen and fracture toughness of CF-ABS by various authors to date with S.D. provided when available

	CF-ABS (BAAM)				
	Test Specimen	**Initial Temp**		**G_{Ic} (J/m^2)**	**S.D.**
Nycz et. al.[111]	DCB	50°C	cold	630	-
			hot	4230	-
		70°C	cold	670	-
			hot	3850	-
		100°C	cold	1560	-
			hot	3420	-
		150°C	cold=hot	5410	-

From the current literature on fracture toughness evaluation there is no consensus on the best approach to fracture testing. Both the behavior of a laminate or of a homogeneous part are observed in FFF parts, depending on the printing parameters, and thus the rheological phenomena at play. The research discussed in this section demonstrates the importance of the print parameters on mesostructure and the subsequent effects on fracture behavior. Further exploration into the laminate versus homogeneous classification of the behavior of FFF parts is needed in order to create the robust standards that are essential to the qualification of materials in FFF applications. While most research to date has focused on mode I, mode II and mixed mode fracture must also be fully characterized to ensure the structural reliability of FFF parts under general loading conditions. Exploration into mode II (G_{IIc}) been initially performed but on a limited basis.[49]

1.5 Scale up of FFF

One of the interesting evolutions of the FFF landscape is the simultaneous advancement of small scale, desktop style printers and industrial scale, Big Area Additive Manufacturing (BAAM) printers. BAAM systems were originally developed by Oak Ridge National Laboratory (ORNL) in conjunction with Lockheed Martin with the goal of printing large components at high rates with lower-cost material.[113] This original technology was primarily proof-of-concept and later ORNL partnered with Cincinnati Incorporated to develop a BAAM system at the prototype stage

which has now become commercially available. This system offered a process that is 10x larger in size and 200x faster than conventional FFF systems.[29] Both desktop printers and BAAM share the overarching print mechanism of layering 2D shapes of molten plastics to create a 3D end part, however the mechanisms and the print strategies used are quite different. Small scale desktop printers utilize filament, which is an extruded wheel of plastic in a set diameter that is then fed into the machine to be melted. In the case of BAAM printers, plastic pellets are fed into a screw extruder where they are heated, melted, and mixed before extrusion. The schematics of the filament-based and pellet-based nozzles are diagramed in **Figure 12**. The major differences here are the mechanisms to obtain the melt temperature and the requirements of print speed and layer times. Despite both printers fabricating parts using the FFF technique, there are significant phenomenological differences relevant to the fracture behavior between parts printed on a large- and small-scale printer.

The relative volume to surface area substantially changes between large scale and small-scale prints creating different build strategy requirements to create a dimensionally accurate and mechanically sound part. As the molten plastic leaves the nozzle, it instantly begins a cooling process from the localized atmosphere in the area directly surrounding the nozzle and the print. In the case of the larger prints, there is a larger volume of heated material creating a higher temperature in the area directly surrounding the print and near the nozzle. However, contrasting with small scale prints, there is a larger amount of free volume compared to print volume, which drastically cools the surface area of the parts. Taking the common nozzle size of a BAAM printer (7.62mm) and the common nozzle size of a desktop FFF printer (0.4mm) and comparing the volume to surface area ratios of a 10mm long extruded section of filament demonstrates the basis for the difference in how the prints interact with a cooling environment. The volume to surface area ratio of the BAAM section was 1.38 whereas the ratio was 0.098 for the desktop printer. Having a higher volume to surface area ratio in an insulating material means more heat is retained to stay above the glass transition temperature. If we invert the 0.098 ratio to calculate surface area to volume ratio, the surface area is nearly 10x that of the volume, creating surface area that is cooled at a much more rapid rate than with BAAM. In these areas the surface polymer chains contract and are frozen into place, building internal stress and shape deformation, commonly referred to as warping.

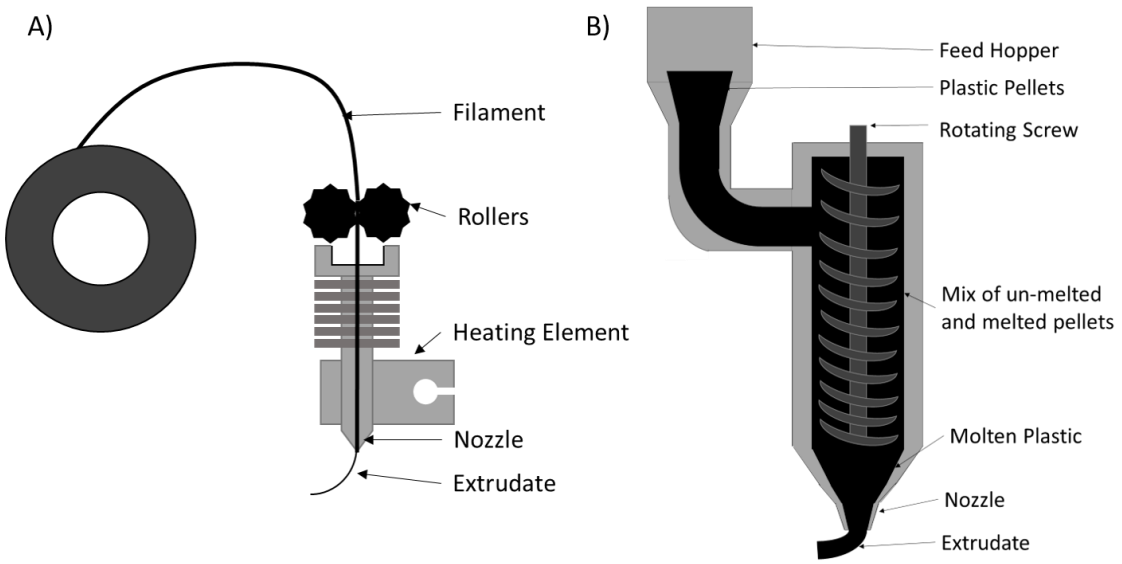

Figure 12. A) Filament based desktop scale FFF schematic B) screw-based pellet extruder in BAAM schematic

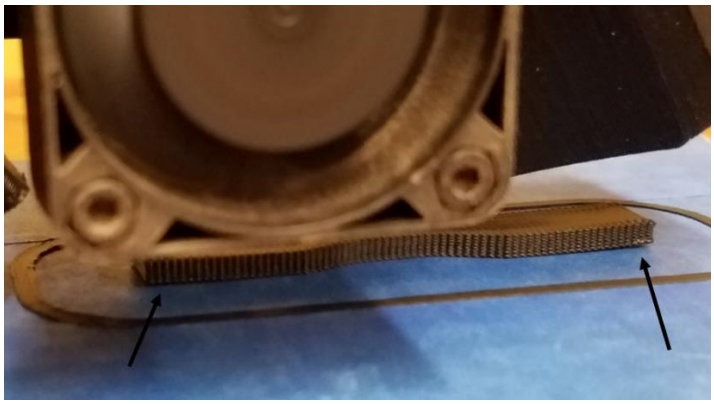

Figure 13. Small scale print evidence of warping as print pulls off the bed during print

This difference between the large- and small-scale prints creates a different optimization for print temperatures and layer times, where larger prints suffer more from sagging and smaller prints suffer more from warping, **Figure 13**. In order to avoid these undesirable effects, build strategies are changed with regards to cooling and patterning, creating a corresponding variation in the mechanical properties including fracture toughness.

In the case of print speed, the overall ability of the print to retain heat influences the optimal pattern for the desired result. In the case of BAAM, building in down time between prints and creating

longer layer times is necessary to avoid the sagging discussed previously, however in the small-scale prints, faster layer times is needed to ensure optimal material mixing at the layers. If the small-scale prints do not experience a certain amount of mixing at the layers, there is a lack of adhesion. The restriction imposed on print quality by layer time is extreme in small scale prints, where surface finish, layer adhesion, and dimensional accuracy are all affected by the layer time. There are a few ways to offset this detrimental effect at the small scale, including changing the nozzle temperature, fan speeds, and utilizing enclosures. These strategies differ on the BAAM printers where the extrudate temperature is dictated by the speed and power of the screw in the single screw extruder system. The temperature and melt quality are influenced by multiple zones of mixing and melting along the screw extruder. Due to the multiple zones of melting, this differs from the small scale where there is a single location where the polymer is melted. That difference results in a difficult comparison of "nozzle temperatures" with regards to scaling up of prints and effects.

Previous work on the BAAM system has followed similar paths to that of desktop printers with research providing insight into the strength and stiffness and improving these properties through the addition of short carbon fibers.[9] The addition of carbon fibers reduced the coefficient of thermal expansion (CTE) and the fiber reinforcement acted as an enabling material to help provide more consistent printing conditions.[113] Beyond the carbon fiber additions for better printing quality, a tamping mechanism was developed by ORNL which provided significantly improved interlaminar strength.[29] Compton et. al. studied the thermal profile of a part during print and from this profile related part distortion to the printing conditions which provided insight into print strategies for these large-scale prints.[114] Compton et. al. concluded that the steady state temperature of the top layer prior to the new layer deposition can be used as an indicator for cracking and warping in thin wall sections.[114] A major takeaway from the aforementioned study was that the ambient temperature in the build chamber had the largest effect on the size of the print that can be printed successfully.[114] In addition to exploring strategies for build optimization, Ajinjeru et. al. studied the rheological behavior of thermoplastic systems with suitability for BAAM printing in mind. This work led to a suggested viscoelastic model to predict the ability to extrude/print materials in question.[115–118] And, much like desktop FFF, fracture mechanics investigations are relatively new to the open literature signaling a shift towards further qualification efforts.

There are numerous similarities between the small scale and BAAM set ups, such as the effects of bed temperature, material quality, fillers, etc that are not discussed here. By pointing out the differences between the set ups, the stage is set for a major distinction moving forward. Despite sharing the same overall concept of layering molten plastic to create a three-dimensional shape, the local area thermodynamics and scale of the two systems greatly impacts layer to layer adhesion. To date, no studies comparing BAAM and desktop fracture toughness of FFF polymers has been published and therefore the printers' effects on fracture toughness at various scales has not been isolated. With the different factors at play, small scale and BAAM printers may need to be categorized and investigated independently, where common approaches to fracture may theoretically make sense across the platforms but do not apply in practice.

1.6 BAAM Fracture

The latest development from ORNL for BAAM systems is substrate temperature control for interlaminar fracture toughness improvement.[119] Kishore et. al. implemented the use of infrared radiation (IR) to preheat the surface of a printed layer to beyond the T_g prior to the next layer being deposited. In order to test the effectiveness of the IR preheat process for interlaminar strength, Kishore et. al. utilized the DCB test discussed earlier. Kishore et. al. calculated the fracture toughness using the LEFM approach. Through the recording of load versus displacement, the energy release rate G was calculated by:

$$G = \frac{3P\delta}{2bA_0} \qquad \text{Eq 11}$$

where b is the sample thickness, P is load, δ is displacement, and A_0 was the initial crack length. Three different lamp conditions and printing speeds were used. The slowest and intermediate speeds showed improved fracture toughness in the conditions which exposed the print to two 500-watt IR lamps at a set height. A large improvement was observed in the fracture toughness when the IR lamps were positioned as close to the print as possible and printed at the slowest speed. In these conditions, introducing a longer time and more heat to the system created a better environment for interlayer diffusion as demonstrated by increased interlaminar fracture toughness. Condition three at the lowest print speed reduced the overall fracture toughness leading to a degradation of ABS conclusion of the high intensity lamps. With higher extrusion temperatures and larger heating provided by IR there was always a reduction in the interlaminar fracture

toughness most likely due to a polymer degradation and introduction of voids within a printed bead.

This research was expanded upon by Nycz et. al. using the same set up of infrared preheating on BAAM printed structures.[112] What Nycz et. al. demonstrated was an experimental set up for in-situ control of the substrate temperature in order to control interlayer mixing. The IR preheating was consistently able to raise the temperature of the previous layer to 150°C and improve the fracture toughness by over 500%. This work demonstrated that raising the substrate temperature beyond the T_g is a viable way to improve the polymer chain mobility across the interface and create a better environment for long range mixing.

As of now, investigations of the fracture toughness of BAAM materials in the open literature is limited as the technology is rapidly expanded and improved. Further fracture toughness specific investigations into BAAM materials is necessary to quantify parametric effects on fracture, such as the specified printing parameters and fracture specimen type. Currently for BAAM, only the DCB specimen type has been utilized in investigating mode I fracture, but further testing of mode II and mixed mode fracture and the associated specimen types must also be addressed. A preliminary investigation to determine G_{IIc} using an End Notch Flexure (ENF) test was unsuccessful when failure occurred through the beads instead of along an interface whether the specimen was oriented for interface failure of sequential layers or bead-bead interface failure within the same layer. A leading cause of inconclusive test results is caused by the inability to achieve crack initiation and propagation along an interface, when the interface is not planar, **Figure 14**. This conclusion is based on a singular set of tests with one material; however, the results indicate the need for a rigorous set of standards for specimen preparation, testing, and results interpretation. While the introduction of new testing standards for strength and stiffness in FFF is already underway, additional research to support fracture standards is needed and the continued investigation of BAAM as a unique FFF subset is important.

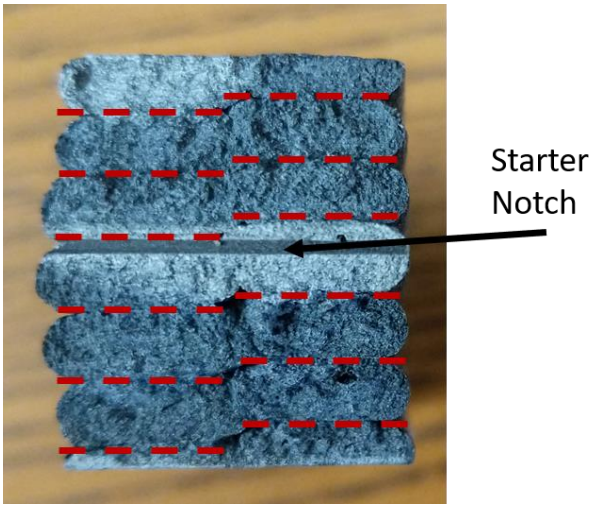

Figure 14. End Notch Flexure (ENF) test specimen where failure occurred through the beads and not at a layer-layer or bead-bead interface

1.7 Conclusions

While this review focused on the FFF of polymers, each of the many types of additive manufacturing (AM) technology including stereolithography,[120,121] selective laser sintering,[36,122] and FFF [123–125] spanning many material types provide advantages and disadvantages, offering a range of manufacturing choices to meet the desired purpose of the part or product. The future of the AM landscape requires further investigation of the fracture behavior of AM parts in order to achieve widespread acceptance for fabricating primary structure. Specific topics for future study identified through this review are listed as follows:

- Fracture toughness evaluations are necessary for material qualification.
- The experimentally obtained properties of an FFF material are sensitive to the test configuration and dimensions as well as the print parameters.
- The quest to better understand the physical complexity that governs the diffusion of polymer chains and entanglement phenomena at the interface in FFF is still ongoing and ever complicated.
- The physics and thermodynamics of molecular chain motion, entanglement phenomena, and diffusion is still not clear, but these are the fundamental sciences governing the joining and adhering of polymer melts.

- Unification of the testing procedures for fracture tests of FFF parts could provide a major boost to those working on physics based multi-scale modeling efforts, where isolating a certain set of rheological boundary conditions at the layer to layer level reduces the overall variance in validation of models to experiments.
- Standardized testing is also essential for material qualification and part certification given the varying testing procedures and nomenclature throughout the literature.
- As the study of the effects of defects becomes more common place, unified testing standards would provide a clearer picture of individual effects of forced or circumstantial defects.
- In addition, further exploration into the classification of the material as homogeneous or as a laminar is important for the design of fracture tests and standards in the future.

1.8 References

[1] B. Brenken, E. Barocio, A. Favaloro, V. Kunc, R.B. Pipes, Fused filament fabrication of fiber-reinforced polymers: A review, Addit. Manuf. 21 (2018) 1–16. https://doi.org/10.1016/j.addma.2018.01.002.

[2] U. Kalsoom, P.N. Nesterenko, B. Paull, Recent developments in 3D printable composite materials, RSC Adv. 6 (2016) 60355–60371. https://doi.org/10.1039/C6RA11334F.

[3] A.K. Sood, R.K. Ohdar, S.S. Mahapatra, Parametric appraisal of mechanical property of fused deposition modelling processed parts, Mater. Des. 31 (2010) 287–295. https://doi.org/10.1016/j.matdes.2009.06.016.

[4] S. Ahn, M. Montero, D. Odell, S. Roundy, P.K. Wright, Anisotropic material properties of fused deposition modeling ABS, Rapid Prototyp. J. 8 (2002) 248–257. https://doi.org/10.1108/13552540210441166.

[5] A. Kantaros, D. Karalekas, Fiber Bragg grating based investigation of residual strains in ABS parts fabricated by fused deposition modeling process, Mater. Des. 50 (2013) 44–50. https://doi.org/10.1016/j.matdes.2013.02.067.

[6] A.R. Torrado, C.M. Shemelya, J.D. English, Y. Lin, R.B. Wicker, D.A. Roberson, Characterizing the effect of additives to ABS on the mechanical property anisotropy of specimens fabricated by material extrusion 3D printing, Addit. Manuf. 6 (2015) 16–29.

https://doi.org/10.1016/j.addma.2015.02.001.

[7] U. Kalsoom, P.N. Nesterenko, B. Paull, Recent developments in 3D printable composite materials, RSC Adv. 6 (2016) 60355–60371. https://doi.org/10.1039/C6RA11334F.

[8] A.C. de Leon, Q. Chen, N.B. Palaganas, J.O. Palaganas, J. Manapat, R.C. Advincula, High performance polymer nanocomposites for additive manufacturing applications, React. Funct. Polym. 103 (2016) 141–155. https://doi.org/10.1016/j.reactfunctpolym.2016.04.010.

[9] L.J. Love, V. Kunc, O. Rios, C.E. Duty, A.M. Elliott, B.K. Post, R.J. Smith, C.A. Blue, The importance of carbon fiber to polymer additive manufacturing, J. Mater. Res. 29 (2014) 1893–1898. https://doi.org/10.1557/jmr.2014.212.

[10] R. Matsuzaki, M. Ueda, M. Namiki, T.-K. Jeong, H. Asahara, K. Horiguchi, T. Nakamura, A. Todoroki, Y. Hirano, Three-dimensional printing of continuous-fiber composites by in-nozzle impregnation. Supporting Information, Sci. Rep. 6 (2016) 23058. https://doi.org/10.1038/srep23058.

[11] X. Wei, D. Li, W. Jiang, Z. Gu, X. Wang, Z. Zhang, Z. Sun, 3D Printable Graphene Composite, Sci. Rep. 5 (2015) 1–7. https://doi.org/10.1038/srep11181.

[12] S. Dul, L. Fambri, A. Pegoretti, Fused deposition modelling with ABS-graphene nanocomposites, Compos. Part A Appl. Sci. Manuf. 85 (2016) 181–191. https://doi.org/10.1016/j.compositesa.2016.03.013.

[13] G. Postiglione, G. Natale, G. Griffini, M. Levi, S. Turri, Conductive 3D microstructures by direct 3D printing of polymer/carbon nanotube nanocomposites via liquid deposition modeling, Compos. Part A Appl. Sci. Manuf. 76 (2015) 110–114. https://doi.org/10.1016/j.compositesa.2015.05.014.

[14] B.G. Compton, J.A. Lewis, 3D-printing of lightweight cellular composites, Adv. Mater. 26 (2014) 5930–5935. https://doi.org/10.1002/adma.201401804.

[15] S. Hwang, E.I. Reyes, K. sik Moon, R.C. Rumpf, N.S. Kim, Thermo-mechanical Characterization of Metal/Polymer Composite Filaments and Printing Parameter Study for Fused Deposition Modeling in the 3D Printing Process, J. Electron. Mater. 44 (2015) 771–

777. https://doi.org/10.1007/s11664-014-3425-6.

[16] D.P. Cole, J.C. Riddick, H.M. Iftekhar Jaim, K.E. Strawhecker, N.E. Zander, Interfacial mechanical behavior of 3D printed ABS, J. Appl. Polym. Sci. 133 (2016) 1–12. https://doi.org/10.1002/app.43671.

[17] Y. Li, H. Shimizu, Improvement in toughness of poly(l-lactide) (PLLA) through reactive blending with acrylonitrile-butadiene-styrene copolymer (ABS): Morphology and properties, Eur. Polym. J. 45 (2009) 738–746. https://doi.org/10.1016/j.eurpolymj.2008.12.010.

[18] M. Vaezi, H. Seitz, S. Yang, A review on 3D micro-additive manufacturing technologies, Int. J. Adv. Manuf. Technol. 67 (2013) 1721–1754. https://doi.org/10.1007/s00170-012-4605-2.

[19] B.N. Turner, R. Strong, S.A. Gold, A review of melt extrusion additive manufacturing processes: I. Process design and modeling, Rapid Prototyp. J. 20 (2014) 192–204. https://doi.org/10.1108/RPJ-01-2013-0012.

[20] P.J. Nuñez, A. Rivas, E. García-Plaza, E. Beamud, A. Sanz-Lobera, Dimensional and Surface Texture Characterization in Fused Deposition Modelling (FDM) with ABS plus, Procedia Eng. 132 (2015) 856–863. https://doi.org/10.1016/j.proeng.2015.12.570.

[21] J.E. Siegel, M.F. Beemer, S.M. Shepard, Automated non-destructive inspection of Fused Filament Fabrication components using Thermographic Signal Reconstruction, Addit. Manuf. 31 (2020) 100923. https://doi.org/10.1016/j.addma.2019.100923.

[22] N.M. DeNardo, Additive manufacturing of carbon-fiber-reinforced thermoplastic composites, 2016. http://search.proquest.com/docview/1849473099?pq-origsite=gscholar.

[23] M. Spoerk, C. Savandaiah, F. Arbeiter, G. Traxler, L. Cardon, C. Holzer, J. Sapkota, Anisotropic properties of oriented short carbon fibre filled polypropylene parts fabricated by extrusion-based additive manufacturing, Compos. Part A Appl. Sci. Manuf. 113 (2018) 95–104. https://doi.org/10.1016/j.compositesa.2018.06.018.

[24] H.L. Tekinalp, V. Kunc, G.M. Velez-Garcia, C.E. Duty, L.J. Love, A.K. Naskar, C.A.

Blue, S. Ozcan, Highly oriented carbon fiber-polymer composites via additive manufacturing, Compos. Sci. Technol. 105 (2014) 144–150. https://doi.org/10.1016/j.compscitech.2014.10.009.

[25] F. Ning, W. Cong, J. Qiu, J. Wei, S. Wang, Additive manufacturing of carbon fiber reinforced thermoplastic composites using fused deposition modeling, Compos. Part B Eng. 80 (2015) 369–378. https://doi.org/10.1016/j.compositesb.2015.06.013.

[26] C.E. Duty, T. Drye, A. Franc, Material Development for Tooling Applications Using Big Area Additive Manufacturing (BAAM), 2015. https://doi.org/10.2172/1209207.

[27] A. Kessentini, G.M.S. Ahmed, J. Madiouli, Design optimization and FE analysis of 3D printed carbon PEEK based mono leaf spring, Micromachines. 10 (2019). https://doi.org/10.3390/mi10050279.

[28] V. Kunc, Advnaces and challenges in large scale polymer additive manufacturing, in: 15th SPE Automot. Compos. Conf., 2015.

[29] C.E. Duty, V. Kunc, B. Compton, B. Post, D. Erdman, R. Smith, R. Lind, P. Lloyd, L. Love, Structure and mechanical behavior of Big Area Additive Manufacturing (BAAM) materials, Rapid Prototyp. J. 23 (2017) 181–189. https://doi.org/10.1108/RPJ-12-2015-0183.

[30] R.T.L. Ferreira, I.C. Amatte, T.A. Dutra, D. Bürger, Experimental characterization and micrography of 3D printed PLA and PLA reinforced with short carbon fibers, Compos. Part B Eng. 124 (2017) 88–100. https://doi.org/10.1016/j.compositesb.2017.05.013.

[31] W. Zhang, C. Cotton, J. Sun, D. Heider, B. Gu, B. Sun, T.W. Chou, Interfacial bonding strength of short carbon fiber/acrylonitrile-butadiene-styrene composites fabricated by fused deposition modeling, Compos. Part B Eng. 137 (2018) 51–59. https://doi.org/10.1016/j.compositesb.2017.11.018.

[32] W. Zhong, F. Li, Z. Zhang, L. Song, Z. Li, Short fiber reinforced composites for fused deposition modeling, Mater. Sci. Eng. A301. 301 (2001) 125–130. https://doi.org/10.1016/S0921-5093(00)01810-4.

[33] A.R. Torrado Perez, D.A. Roberson, R.B. Wicker, Fracture surface analysis of 3D-printed tensile specimens of novel ABS-based materials, J. Fail. Anal. Prev. 14 (2014) 343–353. https://doi.org/10.1007/s11668-014-9803-9.

[34] J. Judson, US Army developing process for using 3D printing at depots and in the field, Def. News. (2020). https://www.defensenews.com/land/2020/02/04/us-army-developing-process-for-using-3d-printing-at-depots-and-in-the-field/.

[35] T. Jackson, Navy Partnershyip Goes to New Depths with First 3D-Printed Submersible, Off. Energy Effic. Renew. Energy. (2017). https://www.energy.gov/eere/articles/navy-partnership-goes-new-depths-first-3d-printed-submersible.

[36] P.K. Jain, P.M. Pandey, P.V.M. Rao, Effect of delay time on part strength in selective laser sintering, Int. J. Adv. Manuf. Technol. 43 (2009) 117–126. https://doi.org/10.1007/s00170-008-1682-3.

[37] J.T. Cantrell, S. Rohde, D. Damiani, R. Gurnani, L. DiSandro, J. Anton, A. Young, A. Jerez, D. Steinbach, C. Kroese, P.G. Ifju, Experimental characterization of the mechanical properties of 3D-printed ABS and polycarbonate parts, Rapid Prototyp. J. 23 (2017) 811–824. https://doi.org/10.1108/RPJ-03-2016-0042.

[38] A.R. Torrado, D.A. Roberson, Failure Analysis and Anisotropy Evaluation of 3D-Printed Tensile Test Specimens of Different Geometries and Print Raster Patterns, J. Fail. Anal. Prev. 16 (2016) 154–164. https://doi.org/10.1007/s11668-016-0067-4.

[39] A.M. Forster, Materials testing standards for additive manufacturing of polymer materials: State of the art and standards applicability, Addit. Manuf. Mater. Stand. Test. Appl. (2015). https://doi.org/10.6028/NIST.IR.8059.

[40] W.M.H. Verbeeten, M. Lorenzo-Bañuelos, P.J. Arribas-Subiñas, Anisotropic rate-dependent mechanical behavior of Poly(Lactic Acid) processed by Material Extrusion Additive Manufacturing, Addit. Manuf. 31 (2020) 100968. https://doi.org/10.1016/j.addma.2019.100968.

[41] M. Mu, C.Y. Ou, J. Wang, Y. Liu, Surface modification of prototypes in fused filament

fabrication using chemical vapour smoothing, Addit. Manuf. 31 (2020). https://doi.org/10.1016/j.addma.2019.100972.

[42] W.H. Ferrell, C.M. Arndt, S. TerMaath, Tensile strength dependence of FFF fiber reinforced ABS on environmental conditioning, Mech. Adv. Mater. Struct. 0 (2020). https://doi.org/10.1080/15376494.2020.1722870.

[43] S.N.A.M. Halidi, J. Abdullah, Moisture and humidity effects on the ABS used in Fused Deposition Modeling machine, Adv. Mater. Res. 576 (2012) 641–644. https://doi.org/10.4028/www.scientific.net/AMR.576.641.

[44] E. Kim, Y.J. Shin, S.H. Ahn, The effects of moisture and temperature on the mechanical properties of additive manufacturing components: Fused deposition modeling, Rapid Prototyp. J. 22 (2016) 887–894. https://doi.org/10.1108/RPJ-08-2015-0095.

[45] F. Arbeiter, M. Spoerk, J. Wiener, A. Gosch, G. Pinter, Fracture mechanical characterization and lifetime estimation of near-homogeneous components produced by fused filament fabrication, Polym. Test. 66 (2018) 105–113. https://doi.org/10.1016/j.polymertesting.2018.01.002.

[46] D. Young, N. Wetmore, M. Czabaj, Interlayer fracture toughness of additively manufactured unreinforced and carbon-fiber-reinforced acrylonitrile butadiene styrene, Addit. Manuf. 22 (2018) 508–515. https://doi.org/10.1016/j.addma.2018.02.023.

[47] N. van de Werken, H. Tekinalp, P. Khanbolouki, S. Ozcan, A. Williams, M. Tehrani, Additively manufactured carbon fiber-reinforced composites: State of the art and perspective, Addit. Manuf. 31 (2020) 100962. https://doi.org/10.1016/j.addma.2019.100962.

[48] F. Ning, W. Cong, Y. Hu, H. Wang, Additive manufacturing of carbon fiber-reinforced plastic composites using fused deposition modeling: Effects of process parameters on tensile properties, J. Compos. Mater. 51 (2017) 451–462. https://doi.org/10.1177/0021998316646169.

[49] W.H. Ferrell, S. TerMaath, Print Parameter Effects on the Fracture Properties of Fiber

Reinforced ABS Composites Fabricated Through Fused Deposition Modeling, in: AIAA SciTech 2019 Forum, 2019. https://doi.org/10.2514/6.2019-0405.

[50] C. Pascual-González, M. Iragi, A. Fernández, J.P. Fernández-Blázquez, L. Aretxabaleta, C.S. Lopes, An approach to analyse the factors behind the micromechanical response of 3D-printed composites, Compos. Part B Eng. 186 (2020) 107820. https://doi.org/10.1016/j.compositesb.2020.107820.

[51] M.H. Wagner, V.H. Rolón-Garrido, The interchain pressure effect in shear rheology, Rheol. Acta. 49 (2010) 459–471. https://doi.org/10.1007/s00397-009-0427-z.

[52] A.Y. Malkin, A. V. Semakov, V.G. Kulichikhin, Modeling macromolecular movement in polymer melts and its relation to nonlinear rheology, Rheol. Acta. 50 (2011) 485–489. https://doi.org/10.1007/s00397-011-0556-z.

[53] H.K. Rasmussen, A constitutive analysis of the extensional flows of nearly monodisperse polyisoprene melts, Polymer (Guildf). 104 (2016) 251–257. https://doi.org/10.1016/j.polymer.2016.05.019.

[54] M.H. Wagner, E. Narimissa, Q. Huang, On the origin of brittle fracture of entangled polymer solutions and melts, J. Rheol. (N. Y. N. Y). 62 (2018) 221–233. https://doi.org/10.1122/1.4995497.

[55] G. Marrucci, F. Greco, G. Ianniruberto, Rheology of polymer melts and concentrated solutions, Curr. Opin. Colloid Interface Sci. 4 (1999) 283–287. https://doi.org/10.1016/S1359-0294(99)90002-X.

[56] H.C. Langelaan, A.D. Gotsis, The relaxation of shear and normal stresses of nematic liquid crystalline polymers in squeezing and shear flows, J. Rheol. (N. Y. N. Y). 40 (1996) 107–129. https://doi.org/10.1122/1.550733.

[57] M.F. Herman, Linear Viscoelastic Response in the Lateral Diffusion Model for Linear Chain Polymer Melts, Macromolecules. 25 (1992) 4931–4936. https://doi.org/10.1021/ma00045a018.

[58] M.L. Becraft, A.B. Metzner, The rheology, fiber orientation, and processing behavior of

fiber-filled fluids, J. Rheol. (N. Y. N. Y). 36 (1992) 143–174. https://doi.org/10.1122/1.550359.

[59] S. Commereuc, Basic Rheology of Polymer Melts: An Introductory Polymer Science Experiment, J. Chem. Educ. 76 (1999) 1528–1532. https://doi.org/10.1021/ed076p1528.

[60] K. Hyun, M. Wilhelm, C.O. Klein, K.S. Cho, J.G. Nam, K.H. Ahn, S.J. Lee, R.H. Ewoldt, G.H. McKinley, A review of nonlinear oscillatory shear tests: Analysis and application of large amplitude oscillatory shear (LAOS), Prog. Polym. Sci. 36 (2011) 1697–1753. https://doi.org/10.1016/j.progpolymsci.2011.02.002.

[61] V. Sharma, G.H. McKinley, An intriguing empirical rule for computing the first normal stress difference from steady shear viscosity data for concentrated polymer solutions and melts, Rheol. Acta. 51 (2012) 487–495. https://doi.org/10.1007/s00397-011-0612-8.

[62] J. Qin, S.T. Milner, Tube diameter of oriented and stretched polymer melts, Macromolecules. 46 (2013) 1659–1672. https://doi.org/10.1021/ma302095k.

[63] T. Sridhar, M. Acharya, D.A. Nguyen, P.K. Bhattacharjee, On the extensional rheology of polymer melts and concentrated solutions, Macromolecules. 47 (2014) 379–386. https://doi.org/10.1021/ma401213r.

[64] A.E. Likhtman, M. Ponmurugan, Microscopic definition of polymer entanglements, Macromolecules. 47 (2014) 1470–1481. https://doi.org/10.1021/ma4022532.

[65] J. Qin, S.T. Milner, Tubes, topology, and polymer entanglement, Macromolecules. 47 (2014) 6077–6085. https://doi.org/10.1021/ma500755p.

[66] Q. Huang, L. Hengeller, N.J. Alvarez, O. Hassager, Bridging the Gap between Polymer Melts and Solutions in Extensional Rheology, Macromolecules. 48 (2015) 4158–4163. https://doi.org/10.1021/acs.macromol.5b00849.

[67] M.H. Wagner, E. Narimissa, V.H. Rolón-Garrido, From melt to solution: Scaling relations for concentrated polystyrene solutions, J. Rheol. (N. Y. N. Y). 59 (2015) 1113–1130. https://doi.org/10.1122/1.4922795.

[68] C. Casavola, A. Cazzato, V. Moramarco, C. Pappalettere, Orthotropic mechanical properties of fused deposition modelling parts described by classical laminate theory, Mater. Des. 90 (2016) 453–458. https://doi.org/10.1016/j.matdes.2015.11.009.

[69] W.H. Ferrell, J. Clement, S. TerMaath, Uniaxial Tensile Testing Standardization for the Qualification of Fiber Reinforced Plastics for Fused Filament Fabrication, Mech. Adv. Mater. Struct. (2019).

[70] P.G. de Gennes, Reptation of a Polymer Chain in the Presence of Fixed Obstacles, J. Chem. Phys. 55 (1971) 572–579.

[71] S. Edwards, The statistical mechanics of polymerized material, Proc. Phys. Soc. 92 (1967).

[72] Y.H. Lin, Number of Entanglement Strands per Cubed Tube Diameter, a Fundamental Aspect of Topological Universality in Polymer Viscoelasticity, Macromolecules. 20 (1987) 3080–3083. https://doi.org/10.1021/ma00178a024.

[73] T.A. Kavassalis, J. Noolandi, New View of Entanglements in Dense Polymer Systems, Phys. Rev. Lett. 59 (1987) 2674–2677. https://doi.org/10.1103/PhysRevLett.59.2674.

[74] L.J. Fetters, D.J. Lohse, D. Richter, T.A. Witten, A. Zirkel, Connection between Polymer Molecular Weight, Density, Chain Dimensions, and Melt Viscoelastic Properties, Macromolecules. 27 (1994) 4639–4647. https://doi.org/10.1021/ma00095a001.

[75] S.T. Milner, Predicting the tube diameter in melts and solutions, Macromolecules. 38 (2005) 4929–4939. https://doi.org/10.1021/ma0355507.

[76] R.H. Colby, M. Rubinstein, Two-Parameter Scaling for Polymers in 9 Solvents, Macromolecules. 23 (1990) 2753–2757. https://doi.org/10.1021/ma00212a028.

[77] Q. Huang, O. Mednova, H.K. Rasmussen, N.J. Alvarez, A.L. Skov, K. Almdal, O. Hassager, Concentrated polymer solutions are different from melts: Role of entanglement molecular weight, Macromolecules. 46 (2013) 5026–5035. https://doi.org/10.1021/ma4008434.

[78] D.E. Dunstan, The viscosity-radius relationship for concentrated polymer solutions, Sci.

Rep. 9 (2019) 1–9. https://doi.org/10.1038/s41598-018-36596-6.

[79] R. Everaers, Topological versus rheological entanglement length in primitive-path analysis protocols, tube models, and slip-link models, Phys. Rev. E - Stat. Nonlinear, Soft Matter Phys. 86 (2012) 1–5. https://doi.org/10.1103/PhysRevE.86.022801.

[80] R. Everaers, K. Kremer, in Model Polymer Networks, 53 (1996) 4–7.

[81] J. Cao, J. Qin, S.T. Milner, Simulating constraint release by watching a ring cross itself, Macromolecules. 47 (2014) 2479–2486. https://doi.org/10.1021/ma500325z.

[82] C.R. Bartels, B. Crist, W.W. Graessley, Self-Diffusion Coefficient in Melts of Linear Polymers: Chain Length and Temperature Dependence for Hydrogenated Polybutadiene, Macromolecules. 17 (1984) 2702–2708. https://doi.org/10.1021/ma00142a045.

[83] M. Doi, S. Edwards, The Theory of Polymer Dynamics, Clarendon Press, Oxford, 1987. https://doi.org/10.1016/0377-0257(87)85036-x.

[84] A. Chremos, C. Jeong, J.F. Douglas, Influence of polymer architectures on diffusion in unentangled polymer melts, Soft Matter. 13 (2017) 5778–5784. https://doi.org/10.1039/c7sm01018d.

[85] W. Paul, G.D. Smith, D.Y. Yoon, Static and dynamic properties of a n-C100H202 melt from molecular dynamics simulations, Macromolecules. 30 (1997) 7772–7780. https://doi.org/10.1021/ma971184d.

[86] C. Jeong, J.F. Douglas, Mass dependence of the activation enthalpy and entropy of unentangled linear alkane chains, J. Chem. Phys. 143 (2015). https://doi.org/10.1063/1.4932601.

[87] A. Chremos, J.F. Douglas, Particle localization and hyperuniformity of polymer-grafted nanoparticle materials, Ann. Phys. 529 (2017). https://doi.org/10.1002/andp.201600342.

[88] Y. Song, Y. Li, W. Song, K. Yee, K.Y. Lee, V.L. Tagarielli, Measurements of the mechanical response of unidirectional 3D-printed PLA, Mater. Des. 123 (2017) 154–164. https://doi.org/10.1016/j.matdes.2017.03.051.

[89] W. Kuhn, Über quantitative Deutung der Viskosität und Strömungsdoppelbrechung von Suspensionen, Kolloid Zeitschrift. 62 (1933) 269–285.

[90] P.J. Flory, Statistical Mechanics of Chain Molecules, Hanser Publications, New York, 1988.

[91] P.G. de Gennes, Scaling Concepts in Polymer Physics, Cornell University Press, Ithaca, 1979.

[92] A.E. Likhtman, Single-chain slip-link model of entangled polymers: Simultaneous description of neutron spin-echo, rheology, and diffusion, Macromolecules. 38 (2005) 6128–6139. https://doi.org/10.1021/ma050399h.

[93] A.E. Likhtman, The tube axis and entanglements in polymer melts, Soft Matter. 10 (2014) 1895–1904. https://doi.org/10.1039/c3sm52575a.

[94] D.J. Read, M.E. Shivokhin, A.E. Likhtman, Contour length fluctuations and constraint release in entangled polymers: Slip-spring simulations and their implications for binary blend rheology, J. Rheol. (N. Y. N. Y). 62 (2018) 1017–1036. https://doi.org/10.1122/1.5031072.

[95] M.E. Shivokhin, D.J. Read, D. Kouloumasis, R. Kocen, F. Zhuge, C. Bailly, N. Hadjichristidis, A.E. Likhtman, Understanding Effect of Constraint Release Environment on End-to-End Vector Relaxation of Linear Polymer Chains, Macromolecules. 50 (2017) 4501–4523. https://doi.org/10.1021/acs.macromol.6b01947.

[96] J. Cao, Z. Wang, A.E. Likhtman, Determining Tube Theory Parameters by Slip-Spring Model Simulations of Entangled Star Polymers in Fixed Networks, Polymers (Basel). 11 (2019). https://doi.org/10.3390/polym11030496.

[97] F.C. Campbell, ed., Fatigue and Fracture: Understanding the Basics, ASM International, Materials Park, OH, 2012.

[98] P.A. Withey, Fatigue Failure of the de Havilland comet I, Eng. Fail. Anal. 4 (1997) 147–154. https://doi.org/10.1016/S1350-6307(97)00005-8.

[99] A.A. Griffith, The phenomena of rupture and flow in solids, Philisophical Trans. R. Soc. London. Ser. A, Contain. Pap. a Math. or Phys. Character. 221 (1921) 163–198. https://doi.org/10.1098/rsta.1921.0006.

[100] G. Irwin, Analysis of stresses and strains near the end of a crack traversing a plate, J. Appl. Mech. 24 (1957) 361–364.

[101] J.R. Rice, A Path Independent Integral and the Approximate Analysis of Strain Concentration by Notches and Cracks, J. Appl. Mech. 35 (1968) 379–386. https://doi.org/10.1115/1.3601206.

[102] G.P. Cherepanov, The propagation of cracks in a continuous medium, J. Appl. Math. Mech. 31 (1967) 503–512.

[103] ASTM International, Standard Test Method for Mode I Interlaminar Fracture Toughness of Unidirectional Fiber-Reinforced Polymer Matrix Composites, Am. Stand. Test. Methods. 03 (2014) 1–12. https://doi.org/10.1520/D5528-13.2.

[104] ASTM International, Standard Test Methods for Plane-Strain Fracture Toughness and Strain Energy Release Rate of Plastic Materials, ASTM J. 99 (2014) 1–9. https://doi.org/10.1520/D5045-14.priate.

[105] T.D. McLouth, J. V. Severino, P.M. Adams, D.N. Patel, R.J. Zaldivar, The impact of print orientation and raster pattern on fracture toughness in additively manufactured ABS, Addit. Manuf. 18 (2017) 103–109. https://doi.org/10.1016/j.addma.2017.09.003.

[106] D.R. Moore, J.G. Williams, A. Pavan, Fracture Mechanics Testing Methods for Polymers, Adhesives and Composites, 1st ed., Elsevier, 2001.

[107] K.R. Hart, E.D. Wetzel, Fracture behavior of additively manufactured acrylonitrile butadiene styrene (ABS) materials, Eng. Fract. Mech. 177 (2017) 1–13. https://doi.org/10.1016/j.engfracmech.2017.03.028.

[108] N. Aliheidari, R. Tripuraneni, A. Ameli, S. Nadimpalli, Fracture resistance measurement of fused deposition modeling 3D printed polymers, Polym. Test. 60 (2017) 94–101. https://doi.org/10.1016/j.polymertesting.2017.03.016.

[109] M. Spoerk, F. Arbeiter, H. Cajner, J. Sapkota, C. Holzer, Parametric optimization of intra- and inter-layer strengths in parts produced by extrusion-based additive manufacturing of poly(lactic acid), J. Appl. Polym. Sci. 134 (2017) 1–15. https://doi.org/10.1002/app.45401.

[110] B.J. Lopes, J.R.M. D'Almeida, Initial development and characterization of carbon fiber reinforced ABS for future Additive Manufacturing applications, Mater. Today Proc. 8 (2019) 719–730. https://doi.org/10.1016/j.matpr.2019.02.013.

[111] K.R. Hart, E.D. Wetzel, Fracture behavior of additively manufactured acrylonitrile butadiene styrene (ABS) materials, Eng. Fract. Mech. 177 (2017) 1–13. https://doi.org/10.1017/CBO9781107415324.004.

[112] A. Nycz, V. Kishore, J. Lindahl, C. Duty, C. Carnal, V. Kunc, Controlling substrate temperature with infrared heating to improve mechanical properties of large-scale printed parts, Addit. Manuf. 33 (2020) 101068. https://doi.org/10.1016/j.addma.2020.101068.

[113] L.J. Love, C. Duty, Cincinnati Big Area Additive Manufacturing (BAAM), Oak Ridge, TN, 2015. https://info.ornl.gov/sites/publications/files/Pub54708.pdf.

[114] B.G. Compton, B.K. Post, C.E. Duty, L. Love, V. Kunc, Thermal analysis of additive manufacturing of large-scale thermoplastic polymer composites, Addit. Manuf. 17 (2017) 77–86. https://doi.org/10.1016/j.addma.2017.07.006.

[115] C. Ajinjeru, V. Kishore, P. Liu, A.A. Hassen, J. Lindahl, V. Kunc, C. Duty, Rheological evaluation of high temperature polymers to identify successful extrusion parameters, Proc. 27th Annu. Int. Solid Free. Fabr. Symp. Addit. Manuf. Conf. (2017) 485–494. http://sffsymposium.engr.utexas.edu/sites/default/files/2017/Manuscripts/RheologicalEvaluationofHighTemperaturePolymer.pdf.

[116] V. Kunc, V. Kishore, X. Chen, C. Ajinjeru, C. Duty, A.A. Hassen, High Performance Poly(etherketoneketone) (PEKK) Composite Parts Fabricated using Big Area Additive Manufacturing (BAAM) Processes, 2016. https://info.ornl.gov/sites/publications/files/Pub72094.pdf.

[117] C. Ajinjeru, V. Kishore, P. Liu, J. Lindahl, A.A. Hassen, V. Kunc, B. Post, L. Love, C.

Duty, Determination of melt processing conditions for high performance amorphous thermoplastics for large format additive manufacturing, Addit. Manuf. 21 (2018) 125–132. https://doi.org/10.1016/j.addma.2018.03.004.

[118] C. Ajinjeru, V. Kishore, X. Chen, J. Lindhal, Z. Sudbury, A. Arabi, A. Hassen, V. Kunc, B. Post, L. Love, The influence of rheology on melt processing conditions of amorphous thermoplastics for Big Area Additive Manufacturing (BAAM), in: 27th Annu. Int. Solid Free. Fabr. Symp., Austin, TX, 2016: pp. 754–762.

[119] V. Kishore, C. Ajinjeru, A. Nycz, B. Post, J. Lindahl, V. Kunc, C. Duty, Infrared preheating to improve interlayer strength of big area additive manufacturing (BAAM) components, Addit. Manuf. 14 (2017) 7–12. https://doi.org/10.1016/j.addma.2016.11.008.

[120] K. Chockalingam, N. Jawahar, U. Chandrasekar, K.N. Ramanathan, Establishment of process model for part strength in stereolithography, J. Mater. Process. Technol. 208 (2008) 348–365. https://doi.org/10.1016/j.jmatprotec.2007.12.144.

[121] A. Sakly, S. Kenzari, D. Bonina, S. Corbel, V. Fournée, A novel quasicrystal-resin composite for stereolithography, Mater. Des. 56 (2014) 280–285. https://doi.org/10.1016/j.matdes.2013.11.025.

[122] I. Shishkovsky, V. Scherbakov, Y. Morozov, Layerwise laser-assisted sintering and some properties of iron oxide core/PEEK shell magnetic nanocomposites, Microelectron. Eng. 146 (2015) 85–91. https://doi.org/10.1016/j.mee.2015.04.030.

[123] A. Bellini, S. Güçeri, Mechanical characterization of parts fabricated using fused deposition modeling, Rapid Prototyp. J. 9 (2003) 252–264. https://doi.org/10.1108/13552540310489631.

[124] O.S. Carneiro, A.F. Silva, R. Gomes, Fused deposition modeling with polypropylene, Mater. Des. 83 (2015) 768–776. https://doi.org/10.1016/j.matdes.2015.06.053.

[125] H. Klippstein, A. Diaz De Cerio Sanchez, H. Hassanin, Y. Zweiri, L. Seneviratne, Fused Deposition Modeling for Unmanned Aerial Vehicles (UAVs): A Review, Adv. Eng. Mater. 20 (2018) 1–17. https://doi.org/10.1002/adem.201700552.

2 Uniaxial Tensile Testing Standardization

2.1 Abstract

Fused filament fabrication (FFF) is a material deposition technique enabling the rapid production of on-demand, customized parts. To support the widespread implementation of FFF into manufacturing supply chains, the qualification of existing and emerging materials for FFF must be standardized, necessitating new and/or modified classification and testing procedures. Current standards do not account for the entire design space capable of FFF technologies. The objective of this investigation is to provide the knowledge needed for development of new standards and practices as demonstrated using the example of the tensile strength of fiber reinforced plastic parts fabricated through FFF. This research is published under the following citation.

2.2 Citation

William H. Ferrell, Jason Clement, and Stephanie C. TerMaath. “Uniaxial Tensile Testing Standardization for the Qualification of Fiber Reinforced Plastics for Fused Filament Fabrication” *Mechanics of Advanced Materials and Structures 0* (2019): 1-20.

2.3 Conclusions

Despite the revolutionary impact of AM technologies, the lack of repeatable testing standards that encompass the complexities unique to printed AM materials has slowed market uptake and limited the overall scope of applicability. New AM standards would provide engineers, scientists, and user/operators the ability to globally compare test results for design and manufacturing, further allowing localized and distributed manufacturing infrastructure to emerge. The ability to account for the anisotropic nature of the part as well as the effects of additives and material blends on the strength and stiffness obtained through tensile testing is needed before widespread adoption of FFF parts for primary load-carrying structure is achieved. In order to create these qualification standards, investigations and reports of processing parameters, orientations, scale-up, and many other complexities are needed while accounting for interacting effects. The interaction of part geometry, orientation, and processing parameters has not been well documented and is necessary to create a standard procedure for testing and production. The primary conclusions of this study are:

- Specimen size and geometry significantly affects strength and repeatability of tensile specimens and a standard FFF specimen configuration must be developed through a comprehensive evaluation. Rather than standardizing dimensions, it may be more applicable to specify the number of beads that are required in the cross-section to achieve geometry independent material properties.
- Continued development and unification of naming and fabrication techniques are needed to compare testing results from disparate sources.
- Controlling layer times and printing processes can lead to both stronger prints and more time efficient fabrication, and extrusion control setting information must accompany test results.
- Printer to printer variability exists, even when fabricating specimens on identical makes and models, and designation of equipment must be considered in the qualification process.

3 Tensile Strength Dependence on Environmental Conditioning

3.1 Abstract

Evaluation of environmental durability is essential for the qualification of polymeric materials used in Fused Filament Fabrication and certification of the manufactured parts. Polymer chain motion at temperatures approaching the glass transition temperature and water ingress into voids impact the response of these materials to load. To investigate these effects, uniaxial tension testing was performed after conditioning specimens under heat or moisture. Results showed that conditioning temperature substantially influences the failure strain in multiple orientations. Both heat, beyond 50ºC, and moisture create increased variability of the specimen response to load, both in ultimate tensile strength and elongation to break. This research is published under the following citation.

3.2 Citation

William H. Ferrell. Corey M. Arndty and Stephanie C. TerMaath. “Tensile Strength Dependence of FFF Fiber Reinforced ABS on Environmental Conditioning” *Mechanics of Advanced Materials and Structures.* 0 (2020): 1-14.

3.3 Conclusions

The effect of heat and moisture on the ultimate tensile strength of fiber reinforced and unreinforced ABS was evaluated within the scope of qualification of polymeric FFF materials. It was found that as the tensile specimens were conditioned at temperatures approaching the T_g, the polymer chain dynamics dictated a slight reduction in the ultimate tensile strength and a significant change in the elongation to break. This finding was consistent between both fiber reinforced and unreinforced polymer systems. In the fiber reinforced specimens, the interfacial bonding was increased due to the increased thermal conductivity provided by the carbon fibers. This provides a decrease in variability but also allows the polymer chains to move more freely past one another at temperature, further reducing the elongation to break. At temperatures of roughly 50% of the T_g, no significant changes in material response to load were observed, providing a potential boundary for the operating temperatures. Specimens subjected to moisture demonstrated an increase in variability and a reduction in tensile strength and elongation to break. However, no trapped water in the voids was found after subjecting the specimens to ambient conditions prior to analysis.

4 A Semi-Circular Bend Specimen for Fracture of BAAM Polymers

4.1 Abstract

Due to the intricate connections between deposition pattern and mechanical performance, it is advantageous to have as few test specimen geometries as possible for studying processing-structure-fracture performance relationships in these BAAM parts. Currently multiple different geometries are being used with testing performed on the parts as if they were a composite laminate or as if they were a homogeneous solid. This study seeks to elucidate the nature of the parts through interlayer and intrabead fracture and evaluate the semi-circular bend specimen for use in fracture mechanics of FFF polymers.

4.2 Introduction

As additive manufacturing techniques such as fused filament fabrication (FFF) make the transition from prototyping to end user part manufacturing, there has been a natural progression of literature developing and promoting the standardization of mechanical testing of these parts. Through the generation of new materials and the adaptations of tensile testing standards, increased understanding of the processing-structure-performance relationships have advanced pertaining to

strength and stiffness. However, due to the highly customizable meso-structures present in FFF parts there has been increased attention paid to the fracture mechanics of these parts.

Current testing of fracture toughness of FFF plastics has primarily focused on the interlaminar and intrabead fracture toughness. These refer to the bead-to-bead and layer-to-layer resistance to crack growth and the through-bead resistance to crack growth respectively. Hart et al performed mode I, or crack tip opening, fracture toughness tests in a three-point bend configuration utilizing the single edge notch bend (SENB) specimen.[1] The interlaminar and intrabead fracture toughness and crack behavior was significantly different in the ABS that Hart et. al. tested due to the reliance on interlaminar toughness on the diffusion between the deposited beads. Several researchers have employed the double cantilever beam (DCB) specimen, which is commonly used for composite laminate parts, for mode I fracture toughness of FFF parts and had good success in obtaining fracture properties of the interlaminar region.[2-5] However, Arbeiter et. al. found that in a fully optimized printing condition of FFF poly-lactic acid SENB specimens that there was an increase in the fracture toughness compared to injection molded parts.[6] This was due to the almost indistinguishable raster patterns signifying an almost fully homogeneous part. Arbeiter et. al. noted that this was purely in the SENB specimen and not in the compact tension (CT) specimen which did not have a perfectly symmetric printing pattern.

There is limited information currently published with regards to fracture testing of FFF parts. The wide range of tests raises concerns of variability in the reported fracture toughness, where there isn't a clear distinction between material property testing and engineered part testing. Due to the large variation in available printing parameters and also different strategies, including print design for repeatability[7] or print design for optimized mixing.[6] Furthermore, the comparison of behavior of the polymer material used in desktop printing and Big Area Additive Manufacturing (BAAM) printing is not well established and the different printing conditions may necessitate specific fracture standards for each. Nycz et. al. performed mode I fracture testing of BAAM printed carbon fiber reinforced acrylonitrile-butadiene-styrene (CF-ABS) using the DCB specimen to investigate the effects of preheating layers.[5] As it pertains to standardization for fracture toughness evaluation, the DCB specimen is only able to obtain the mode I interlayer fracture toughness necessitating multiple other specimens to test for mode II, or shear, fracture and intrabead fracture.

Through the use of a semi-circular-bend specimen (SCB) in a three-point bend test configuration, a single specimen geometry can be used to determine the multiple modes and multiple regions of fracture toughness present in FFF parts. The reduction of geometry specific testing provides unity in the manufacturing of parts and the testing of parts that will provide a consistent basis for varying the processing conditions and capturing isolated effects.

4.3 Materials and Methods

4.3.1 Materials

ABS base polymer with 20 weight % (wt. %) carbon fiber reinforcement was printed through the Big Area Additive Manufacturing (BAAM) system at Oak Ridge National Lab. The BAAM utilizes polymer pellets and a single screw extruder to melt and homogenize the polymer before the deposition. The polymer is deposited onto a heated ABS based plastic sheet that is adhered to the metal heating platform to ensure part stability during the printing process. Rectangular plaques with varying sizes and printing parameters were manufactured to provide a robust test platform to elucidate the material behavior and the fracture toughness. Smaller plaques that were 0.66 m x 0.254 m x 0.04524 m, length by height by width, were printed at 220C, 230C, and 240C with a 90 second layer time. Then larger plaques that were 1.5 m x 0.254 m x 0.0381 m, length by height by width, were printed all with the same extrusion temperature but with a 2-minute, 4-minute, and 6-minute layer time.

4.3.2 Specimen Geometry

The SCB specimen chosen was based on the asphalt mixture cracking resistance testing standard, ASTM D8044, **Figure 15**.[8-11] Due to the simple nature of manufacturing multiple geometries were tested depending on the thickness of the printed plaques.

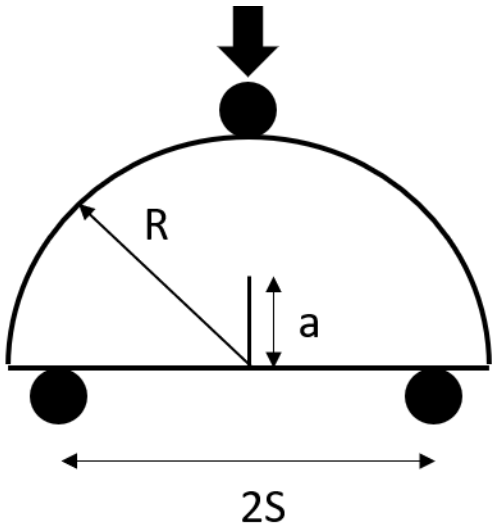

Figure 15 SCB specimen geometry where B is width, R is radius, S is span, and a is the crack length [12]

In order to keep the specimens within the plane-strain criteria, the single edge notch bend (SENB) for mode I fracture toughness standard was referenced. Based on this standard, a width to thickness ratio of 1:1 up to 4:1 was considered plane strain. Based on this, a maximum thickness to width ratio of 2:1 was prepared to ensure plane-strain but minimize plastic deformation at the rollers due to compression.

For plaques printed with a 2-bead configuration, width roughly equaling 15.875 mm post printing, a specimen thickness of 33.02mm was used. This 2-bead width configuration was printed for both the 20 wt. % CF-ABS. For the 4-bead width configuration, roughly equaling 38.1 mm width, a specimen thickness of 76.2 mm was used to maintain this 2:1 ratio.

4.3.3 Mechanical Testing

Testing was performed on an MTS Cirterion 45 electomechanical load frame with a 10kN load cell and a 100kN load cell based on the specimen size. For the 33.02 mm radius specimens the 10kN load cell was used with a maximum load of 5kN achieved, and for the 76.2 mm radius specimens the 100kN load cell was used with a 20kN maximum load achieved. The 100kN load cell was also utilized for the SENB specimens. Testing was performed in the three-point bend configuration. Loading was applied at 0.5 mm/min.

Two orientations, **Figure 16**, were used to determine the interlayer and intrabead fracture toughness in mode I. For mode I fracture, the notch and starter crack were oriented perpendicular to the bottom of the specimen where the crack grew vertically towards the top roller. The starter crack was made with a razor blade within the notch made with a bandsaw. For interlayer G_{Ic} the layers were oriented vertically and for the intrabead GIc the layers were oriented perpendicular, **Figure 16**. The span was set to be 80% of the specimen diameter for mode I fracture to achieve the highest tensile stress at the crack tip, **Figure 15**.

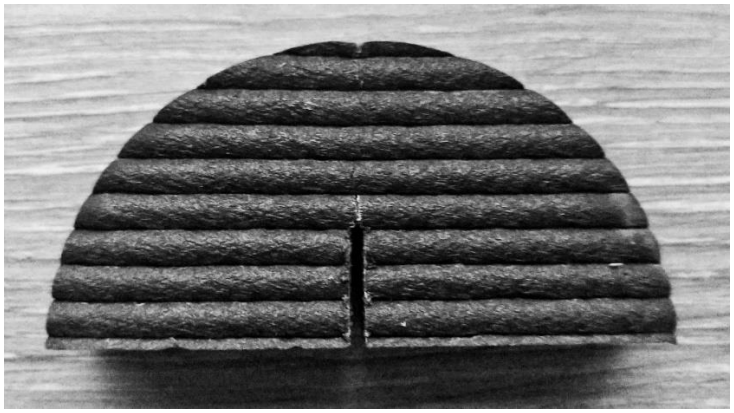

Figure 16 Intrabead fracture SCB specimen orientation

This specimen also is capable of a mixed mode I/II testing configuration by tilting the notch at specified angles to achieve the particular loading case necessary. Multiple bead orientations were used to explore the interlayer and intralayer mixed mode fracture

4.3.4 Fracture Theory

Through the use of the SCB specimen the fracture toughness of the BAAM CF-ABS material was explored. For the evaluation of fracture properties in FFF materials, the variability in layer adhesion and location, as well as the development of plastic zones in the FFF parts create difficulty in consistent evaluation. In the BAAM CF-ABS material the fracture toughness was evaluated using both linear elastic fracture mechanics and elastic-plastic fracture mechanics.

Linear elastic fracture

For linear elastic materials, the critical mode I stress intensity factor Kic can be calculated using equation 1,

$$K_I = Y' \left(\frac{P\sqrt{\pi a}}{2RB}\right) \quad \text{Eq 1.}$$

where P is the load, a, R, and B, are the crack length, radius, and the width, respectively. Y' is the normalized stress intensity factor for the SCB specimen and for the span to radius ratio of 0.8, which is used for mode I, can be written as:

$$Y' = 5.6 - 22.2\beta + 166.9\beta^2 - 576.2\beta^3 + 928.8\beta^4 - 505.9\beta^5 \quad \text{Eq 2.}$$

where beta is the a/R ratio. Using the P maximum from the load displacement plots, the critical stress intensity factor K_{Ic} can be determined. From the K_{Ic} the critical strain energy release rate, G_{Ic} (units of J/m^2) can be calculated, under the assumption of linear-elastic behavior and straight crack propagation. In the case of linear-elastic failure, the G_{Ic} can be related to the critical elastic-plastic strain energy release rate, J_{Ic} (units of J/m^2) through

$$J_{Ic} = G_{Ic} = K_{Ic}^2 \left(\frac{1-\nu^2}{E}\right) \quad \text{Eq 3.}$$

where E is the elastic modulus and ν is the Poisson's ratio of the material. This relationship allows the comparison of the calculated critical stress intensity factors between ductile and brittle materials.

Elastic-plastic fracture

Materials that exhibit ductility in the crack tip region cannot be analyzed using the linear elastic fracture framework. Two methods of calculating the J_{Ic} were evaluated with regards to the use of the SCB specimen on BAAM plastic specimens. The initial method was through the J calculations presented with testing of asphalt SCB specimens. This involved the comparison of the max load of SCB specimens with different initial notch depths. The linear regression of the plot of strain

energy, or the area under the load displacement curve, versus initial notch depth is divided by the width of the specimens to provide J_c from:

$$J_c = -\left(\frac{1}{b}\right)\left(\frac{dU}{da}\right) \quad \text{Eq 4.}$$

where U is the strain energy to failure, b is the sample width, and *a* is the notch depth.

The second method of calculating J_{Ic} was through the comparison and adaptation of the ASTM D6068 standard for determining J-R curves of plastic materials to the SCB test and the FFF material. Through the use of high speed and high-resolution cameras commonly used in digital image correlation (DIC), the crack advancement path and length were monitored in order to use the J-R curve method in the ASTM D6068 standard. In the test methodology from the ASTM D6068 standard, a specimen with an initial crack length a_0 is loaded to introduce a crack propagation of length delta *a* with the resulting load displacement curve used to calculate the strain energy U. The associated J values are calculated according to

$$J = \frac{\eta U}{b(W-a_0)} \quad \text{Eq 5.}$$

Where η is a geometric constant, b is sample width, W is sample height which is equal to R in the case of this adaptation. The geometric constant η used in this test was the same for the single edge notch bend specimen, value of 2, due to no current constant in the standard for the SCB specimen. This shape factor has been calculated for different specimens through the use of finite element analysis but was not explored in this study. The calculated values of J are plotted against the crack advancement Δ*a* and fitting a power law in the form of

$$J^{fit}(\Delta a) = C_1 \Delta a^{C_2} \quad \text{Eq 6.}$$

where C_1 and C_2 are the fitting parameters. On the same set of axes, an offset blunting line is plotted to account for the development of the plastic zone in front of the crack tip. This offset blunting line is created from

$$J^{blunt}(\Delta a) = 2\sigma_y(\Delta a - \varepsilon) \quad \text{Eq 7.}$$

where σ_y is the yield stress of the material and ε is the offset value. The offset value of 0.2 mm was applied based on the work done by Lu et. al. [13] The intersection of the blunting line with the J-R curve is the critical elastic-plastic strain energy release rate, J_{Ic}.

4.4 Results

4.4.1 Mode I Intrabead Fracture

The initial orientation was selected to test for intrabead fracture, **Figure 16**. Due to cutting location, the notch ended at various points within the printed beads. The effects of the notch tip location in the bead was slightly tied to the overall behavior of the specimens under load in this configuration. In particular, sample 7, 10, 11, 14 and 15 demonstrate the notch ending at either the topmost or bottom-most section of the bead. In the associated area adjusted stress versus displacement curve, these specimens demonstrated a higher modulus and higher failure load than in the specimens with the notch ending in the middle of a bead. Despite sample 6-10 having a higher printing temperature than specimens 11-15, the overarching behavior of the specimens remained fairly similar.

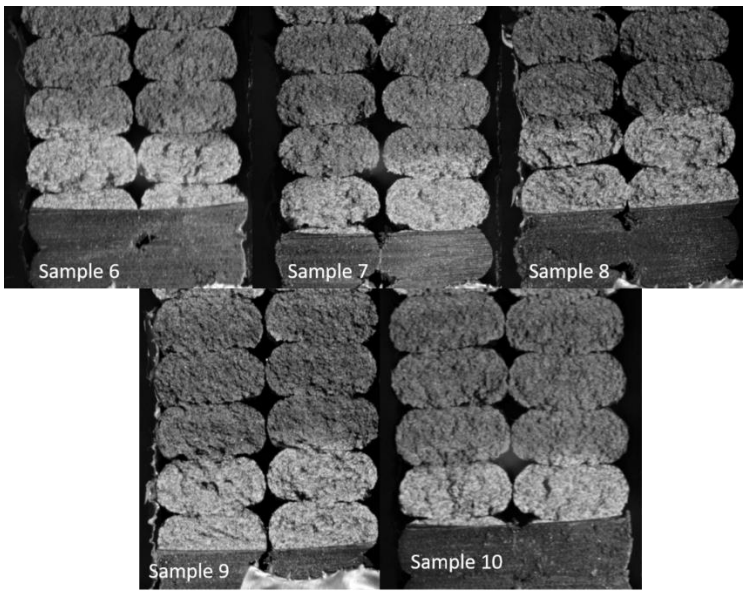

Figure 17 Fracture surface of the SCB 33.02mm radius specimens printed at 230°C.

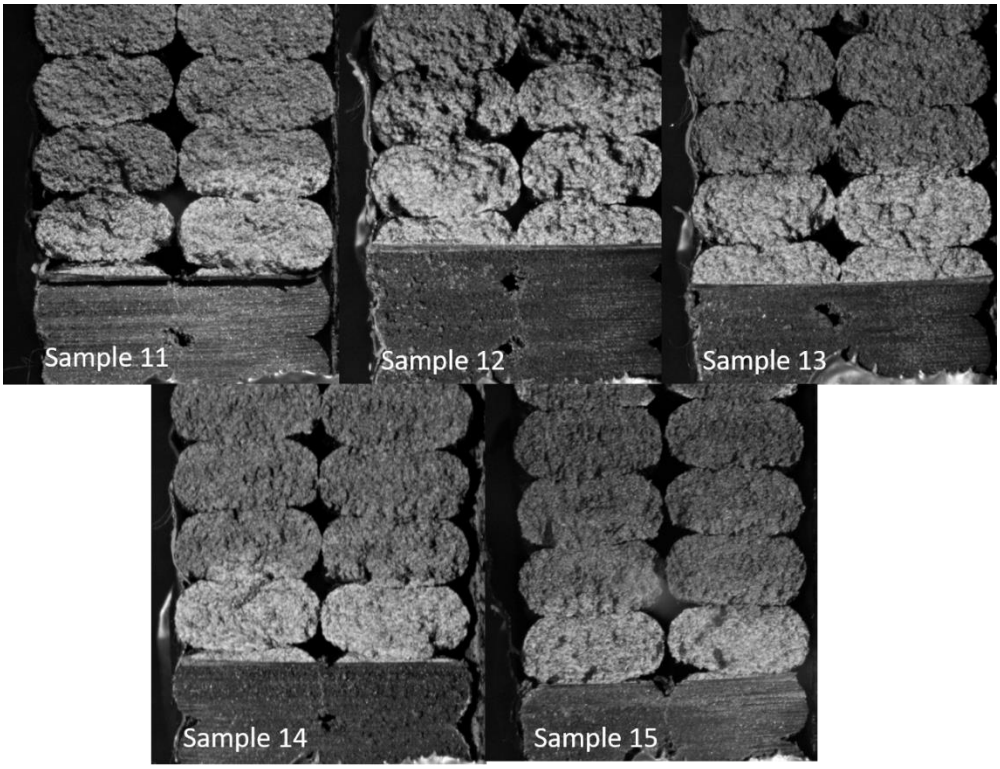

Figure 18. Fracture surface of the SCB 33.02mm radius specimens printed at 220°C. Due to cutting location, the notch ended at various points within the printed beads

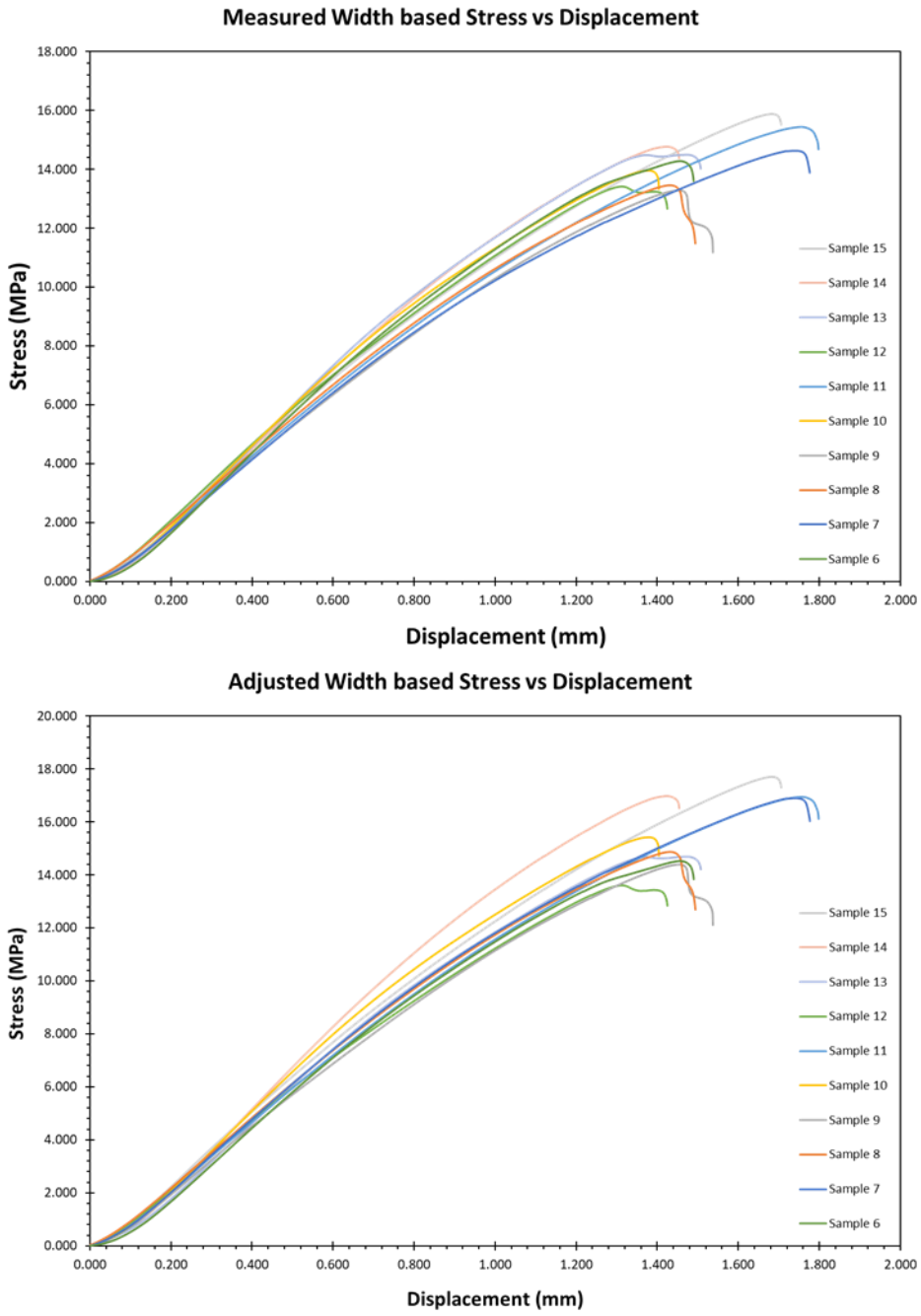

Figure 19. Noticeable effects and variations occur when adjusting the width of the specimen based on the cross section of the figures above

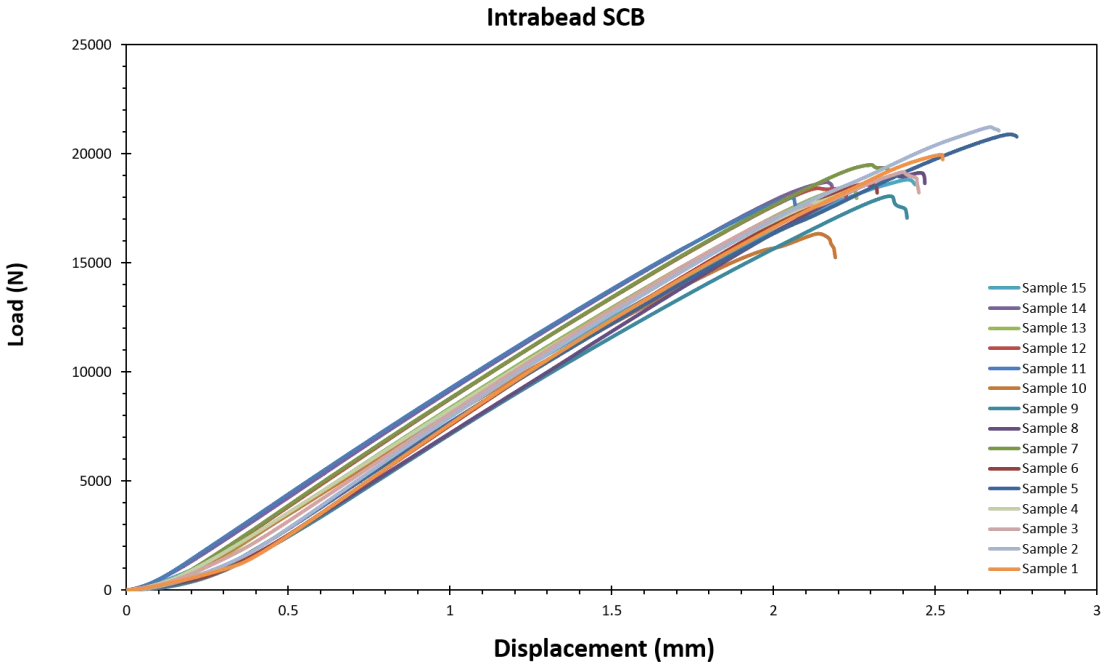

Figure 20. Load versus displacement for mode I fracture toughness intrabead

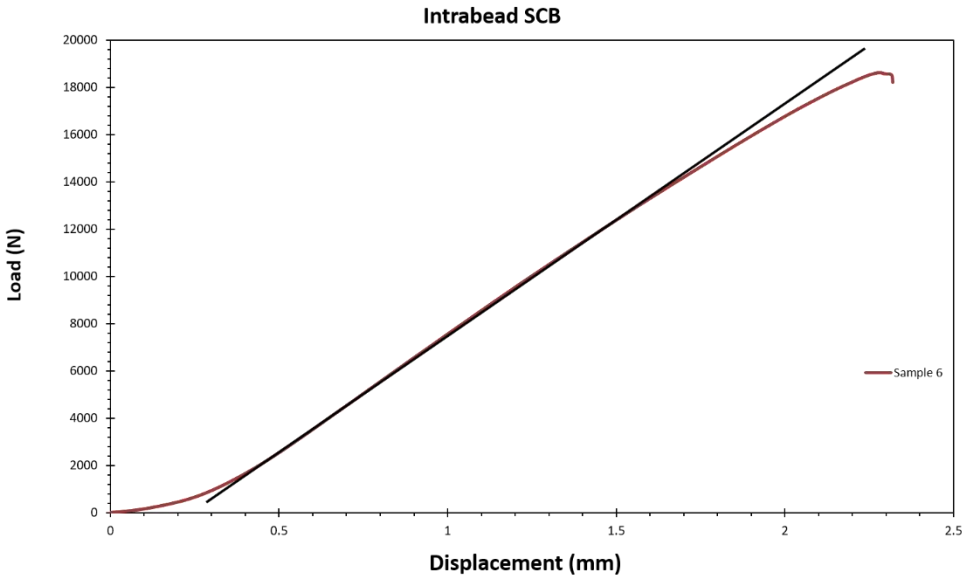

Figure 21. Deviation from linearity example with straight line applied to load versus displacement curve

4.4.2 SCB Specimens from 1.5m Plaque

In the larger plaque specimens for intrabead failure, the preliminary testing shows little plasticity and very consistent failure, **Figure 20**. In these tests, the specimen width is 38.1 mm, and the thickness is 76.2 mm. There was a significant decrease in the plasticity of the part and a reduction in the visual deformation near the rollers under loading. The load displacement behavior and sudden failure demonstrate brittle behavior with a small region of stable crack growth. The small deviation from linearity generally marked the region where the crack begins to form. To observe the deviation from linearity, a straight line was plotted over the data following the slope of the load versus displacement curves, **Figure 21**.

From equations 1 and 2, the normalized SIF and then subsequently K_{Ic} and G_{Ic} were calculated. **Table 4** and **Table 5** outline the slight variation in the initial crack length and then the critical crack length and both of these values were used in the calculation of the G_{Ic}. This comparison provided a slight increase in the calculated G_{Ic} which is to be expected with a slightly longer crack length at failure.

Table 4. Specimen geometry values and fracture toughness calculated, with standard deviation (STD), calculated using the initial crack length a

	6 min layer	STD	4 min layer	STD	2 min layer	STD
a (m)	0.030	4.07E-04	0.030	1.66E-03	0.030	1.03E-03
R (m)	0.076	1.28E-04	0.076	2.15E-04	0.076	8.93E-05
B (m)	0.037	1.93E-04	0.037	2.40E-04	0.038	1.73E-04
Y1	5.099	4.40E-02	5.130	1.78E-01	5.143	1.08E-01
β	0.394	6.00E-03	0.395	2.27E-02	0.399	1.39E-02
P (N)	20366	729	18323	1106	18465	289
K_{Ic} ($Mpa*m^{1/2}$)	5.58	0.176	5.09	0.117	5.09	0.137
G_{Ic} (J/m^2)	2292	145	1905	89	1903	102

Table 5. Specimen geometry values and fracture toughness calculated, with standard deviation (STD), calculated using the critical crack length a_c.

	6 min layer	STD	4 min	STD	2 min	STD
a (m)	0.038	1.38E-03	0.040	2.66E-03	0.040	1.18E-03
R (m)	0.076	1.28E-04	0.076	2.15E-04	0.076	8.93E-05
B (m)	0.037	1.93E-04	0.037	2.40E-04	0.038	1.73E-04
Y1	5.099	4.40E-02	5.130	1.78E-01	5.143	1.08E-01
β	0.394	6.00E-03	0.395	2.27E-02	0.399	1.39E-02
P (N)	20366	729	18323	1106	18465	289
K_{Ic} (Mpa*m1/2)	6.27	0.169	5.90	0.138	5.82	0.143
G_{Ic} (J/m^2)	2895	156	2556	120	2492	122

From the initial analysis of the slight deviation from linearity, a comparison and testing of the J-integral method as compared to the G_{Ic} calculation and evaluation was performed. In order to calculate the J-integral method, several different methods were used in order to explore the applicability to this materials system. The initial analysis of the J-integral to determine J_{Ic} was to compare the load carrying capacity of the system at two different initial notch lengths. The comparison of the 0.3*R and 0.4R, shown in **Figure 22**, greatly overestimated the J_{Ic} providing a value of 38.7 kJ/m2 which was over ten times the values from the G_{Ic}. In perfectly linear elastic isotropic brittle materials, the J_{Ic} reduces to the G_{Ic}. Based on the load displacement, it is highly unlikely that the toughness is this different with the apparent semi-brittle nature. The specified use of maximum load, for the integration point for total strain energy, as compared to the load where the crack begins to propagate is a major source of error when comparing this with other methods.

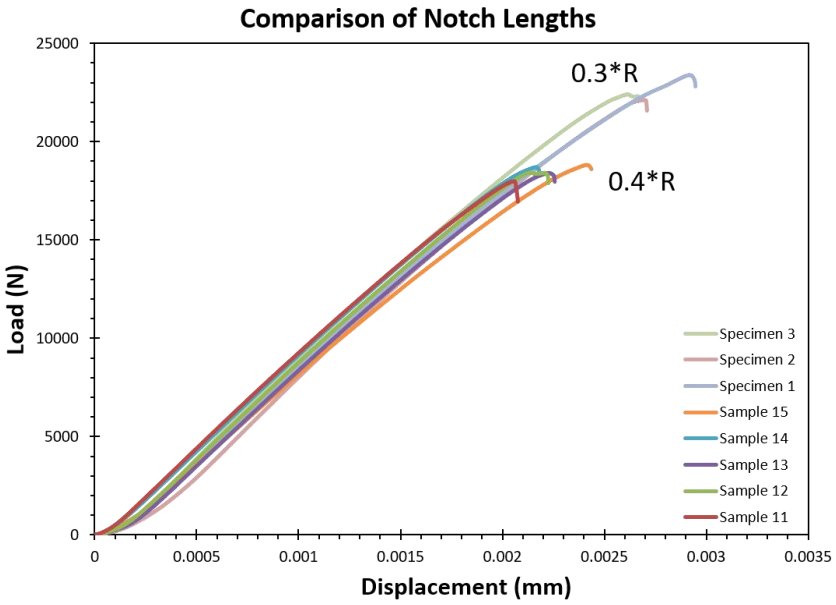

Figure 22. Comparison of the load carrying capacities of the 0.3*R and 0.4*R notch lengths.

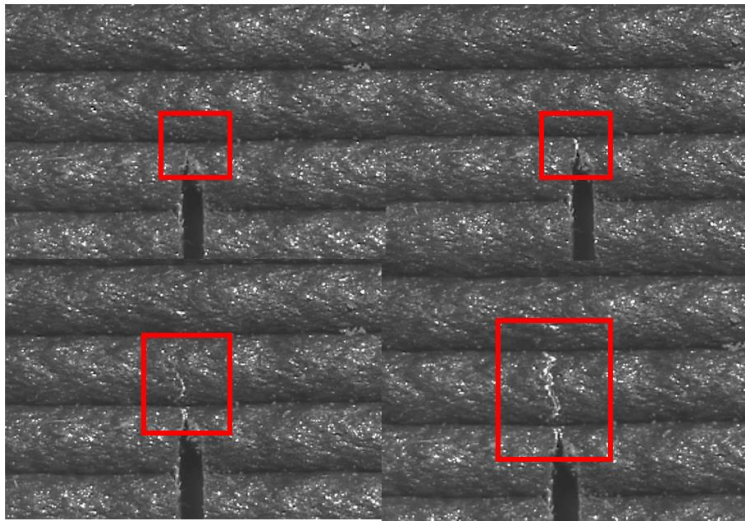

Figure 23. DIC images of crack growth during specimen loading. From top left to bottom right, the crack growth can be seen in the red boxes.

Based on this, the creation of J-R curves, or the J versus resistance, as the crack propagates was created in order to better evaluate the Jic. Based on the shape and size of the SCB specimen, using sets of specimens and loading to certain displacements for crack growth created several challenges. To alleviate this, digital image correlation was used to track crack growth so a J-R curve could be

created for a single specimen as it underwent load to failure, **Figure 23**. An example of the created J-R curve, provided in **Figure 24**, demonstrates the sensitivity of the method on the measurement of crack advancement throughout the test. Because of the DIC limitations, having only surface imaging of the crack, there is inherent error in these curve fits and subsequently the calculation of Jic. The benefit of this method though is the ability to measure the Jic for each specimen rather than relying on multiple different specimens being loaded to different points in order to obtain the Jic. In the evolution of the fracture testing for FFF, the ability to measure specimen to specimen variability becomes increasingly important for qualification purposes. Single test geometries and tests allow for better understanding of printing parameter effects on the tested fracture toughness values.

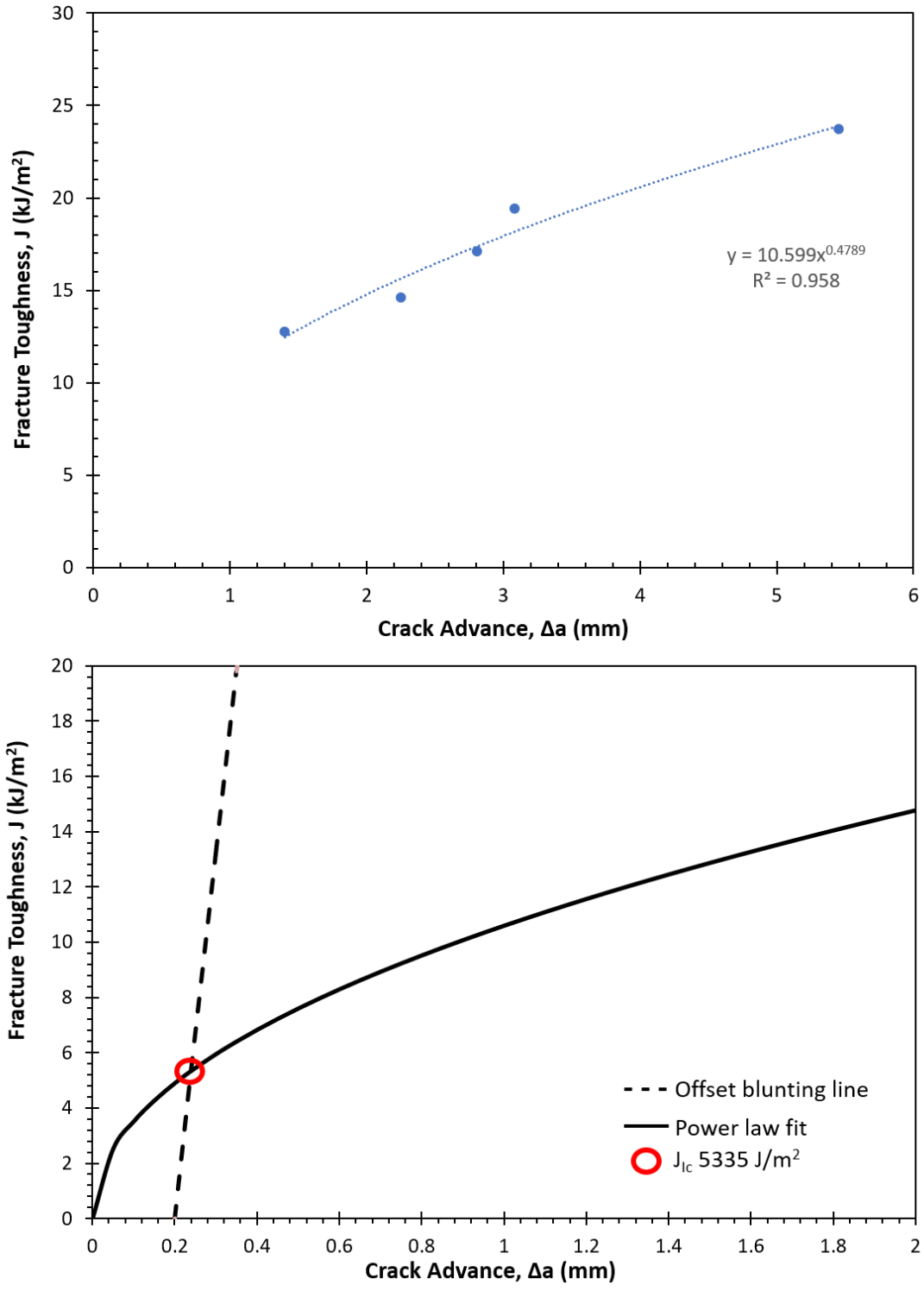

Figure 24. J-R curve for intrabead SCB specimen 14, as an example.

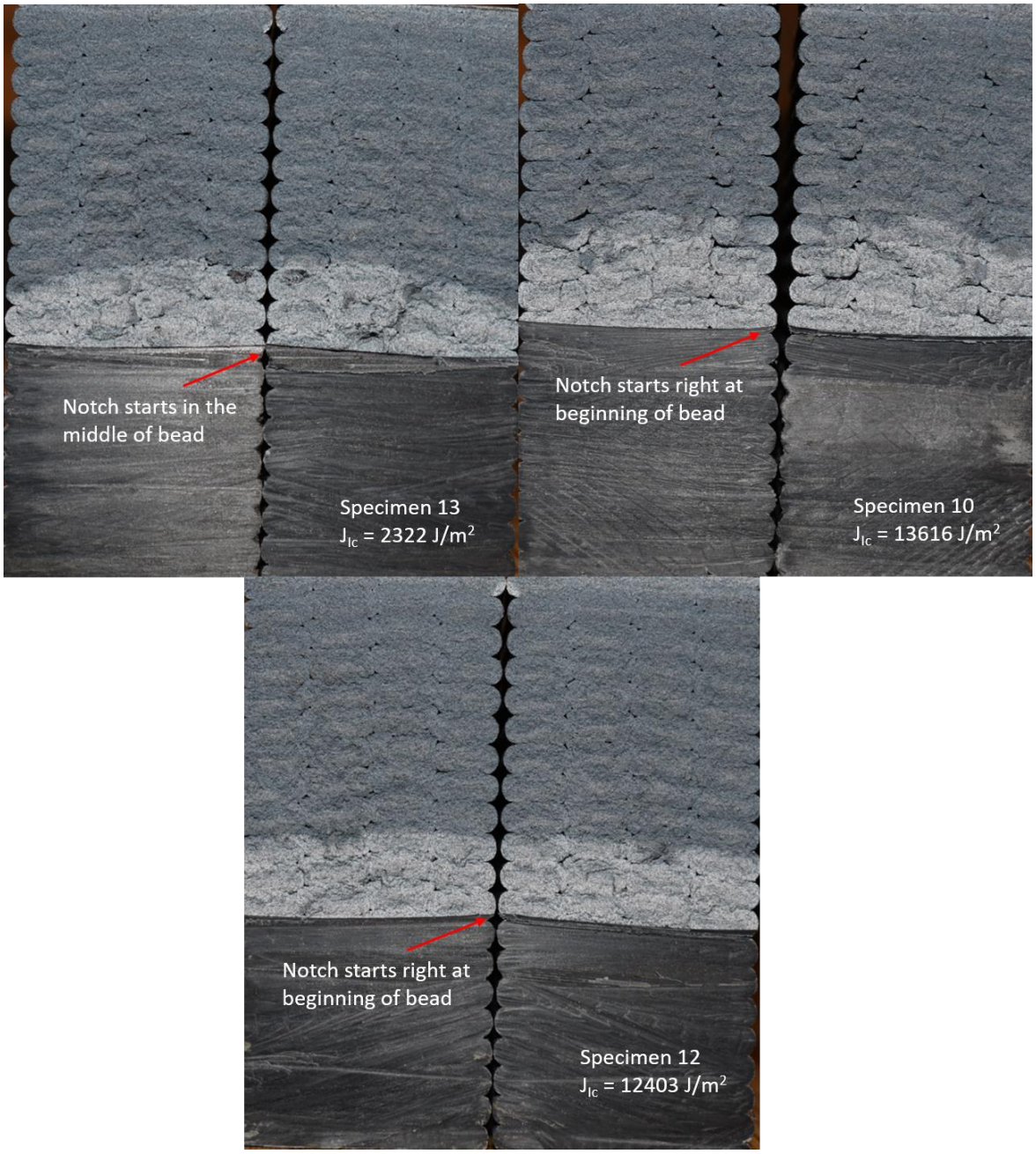

Figure 25. Fracture toughness dependence on initial notch location

Due to the heavy reliance of the J_{Ic} on the crack advance measurements the individual calculation of the J_{Ic} of each specimen is shown on the fracture surface of several notable specimens. The fracture surfaces of the SCB specimens also show some reliance of the crack on the bead locations and the shape of the initial notch, **Figure 25**.

For the interlayer specimen tested, the load displacement curve is seen in **Figure 26**. Based on the calculated fracture toughness through the bead, the maximum load should be predicted if the nature of the specimen is homogeneous with systematic voids. However, if the interlayer properties are significantly different than in the intrabead properties then the laminate nature of the material can be confirmed with reasonable certainty. The overall behavior of the material is slightly more linear in nature but still shows a little bit of yielding before failure.

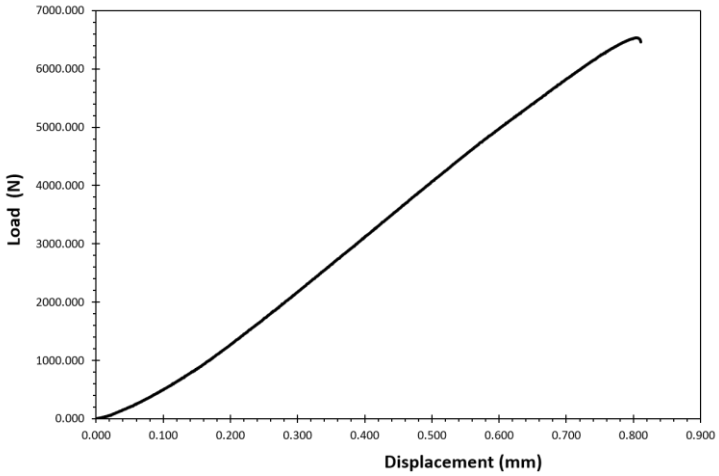

Figure 26. Interlayer SCB specimen load displacement plot showing very minimal deviation from linearity.

4.5 Discussion

4.5.1 Comparison of G and J

In this particular testing method, the overall behavior was surprisingly linear despite being a plastic material. However, in the comparison of G and J there existed differences that lead to the conclusion that for precise analysis and predictive modeling, the J integral approach should be performed. The overall average intrabead J_{Ic} of the CF-ABS BAAM specimens was calculated to be 7564 J/m^2 which is within reason for the fiber reinforced ABS material where the pure ABS material demonstrated a J_{Ic} of 3500-5500 J/m^2. This is compared to the average G_{Ic} of 2648 J/m^2 which is similar to the calculated toughness of hot press molded SENB tests of 15 wt% CF reinforced ABS, which was 3090 J/m^2. For the intrabead fracture toughness tests, the crack generally began to propagate at around 12kN to 14kN and the specimen sustained loads on average

of 18kN-20kN. This is a large amount of non-linear load that could be accounted for in the material testing. With that in mind though, the current test set up explored in this work could not fully guarantee the load at which the crack began to propagate due to only characterizing surface crack growth. The full adherence of specimen testing to ASTM D6086 would be needed in order to more adequately qualify a material based on mode I fracture toughness through a deposited bead.

However, this test showed a self-contained and highly repeatable set up to determine the G_{Ic} with relative ease and accuracy that could be used for multiple orientations and expanded to mixed mode and pure mode II fracture. The cracks generally grew between 5-8mm, or roughly 10.9% to 17% of the ligament length, before sudden failure. This fairly brittle behavior demonstrates that it is not entirely unreasonable to categorize the fracture toughness by G_{Ic}.

4.5.2 Layer Time effect on fracture

The relative ease of measuring the G_{Ic} and the repeatable nature allowed for the comparison of three different layer times, 2 min, 4 min, and 6 min, with relatively low error. From these tests, **Table 4** and **Table 5**, the G_{Ic} shows slightly higher values for the 6 min layer time, roughly 16% higher. This behavior could be because of the slightly more pronounced raster voids in the material. These voids, while not appearing to cause significant impact on the intrabead failure, could be concentrating and arresting the stresses in front of the crack tip. As the pressures in front of the crack tip go from a large area to a smaller area, following the ellipse of the bead, and then back to a larger area, more load capacity could be held after the initial crack initiation. This is seen in specimens where the notch started at the beginning or end of a bead.

4.5.3 Interlayer Fracture Toughness

The interlayer G_{Ic} value using the layer to layer Z-axis modulus of 2.13 GPa, from the work by Duty et. al., [14] was calculated to be 1515 J/m^2 with a Poisson's ratio of 0.35. However, for small scale evaluations of the CF-ABS material demonstrate a Poisson's ratio as low as 0.2 depending on orientation. Altering the calculation with this Poisson's ratio in mind produces a G_{Ic} value of 1657 J/m^2, which while lower than the intrabead, is still very close to the calculated G_{Ic} of the intrabead properties. Both of these values are well within the range of the interlaminar fracture toughnesses explored by Nycz et. al. using a dual cantilever beam test to explore layer preheating. The values provided by Nycz et. al. show toughness values of 1560J/m^2 for layers roughly the temperature expected for plaques of this size.[5]

4.5.4 Characterization of BAAM Parts

The important conclusion from comparing the work by Nycz and the above testing, is that when adjusting for the known modulus differences along the deposited bead and across layers, the fracture toughness values are relatively close. With the adjustment of processing conditions, the difference shrinks with the maximum interlaminar fracture toughness achieved as 5410 J/m^2.[5] Based on the fracture surfaces, **Figure 27**, and the results that show a shrinking of the difference in intrabead and interlayer G_{Ic}, the material could be categorized as a transversely isotropic material with distinct moduli and distinct material properties within the bead and at the interface. From **Figure 27**, the fracture surfaces demonstrate consistent crazing symptomatic of plastic deformation only in the middle of the beads, with a lack of this present at the interfaces of beads and layers. From this, there is a material difference within the beads and at the layers, however this could be a function of the processing conditions chosen for this particular set of tests. Further evaluation of more optimal printing conditions should be performed in order to fully categorize the homogeneity of the parts.

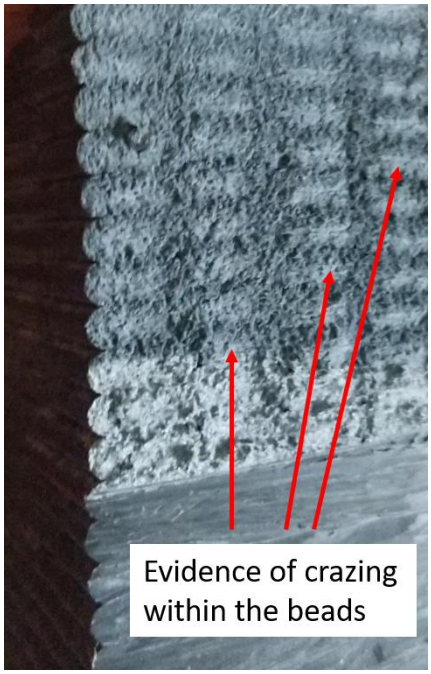

Figure 27. Crazing within the beads but not at the interface demonstrates different material behavior and properties in the various locations

4.6 Conclusions

The SCB test specimen has been shown to reasonably capture the G_{Ic} and J_{Ic} of both the interlayer and the intrabead properties of BAAM manufactured specimens. This test provides the ability to obtain interlayer properties and intrabead properties with the same specimen geometries, reducing the variability of shape effects and manufacturing approaches. The ease of manufacturing also allows for more specimens to be tested without the strict crack insertion requirements of current interlaminar fracture toughness tests. Expanding this test to measure the mixed mode I/II and pure mode II requires only adjusting the crack angle and the span distance to systematically test the effect of processing conditions and deposition strategies on the fracture properties of the material. However, due to the size and shape of the specimens, the production of a J-R curve becomes slightly more difficult in order to achieve cryofracture to fully determine the location of the crack advancement per force applied. Ultimately the SCB specimen has the potential to provide a unified specimen to investigate the effects of multiple processing conditions and strategies to further explore the processing/fracture relationships within BAAM manufactured plastics.

4.7 References

[1] Hart, K. R. & Wetzel, E. D. Fracture behavior of additively manufactured acrylonitrile butadiene styrene (ABS) materials. *Eng. Fract. Mech.* **177**, 1–13 (2017).

[2] Spoerk, M. *et al.* Anisotropic properties of oriented short carbon fibre filled polypropylene parts fabricated by extrusion-based additive manufacturing. *Compos. Part A Appl. Sci. Manuf.* **113**, 95–104 (2018).

[3] Young, D., Wetmore, N. & Czabaj, M. Interlayer fracture toughness of additively manufactured unreinforced and carbon-fiber-reinforced acrylonitrile butadiene styrene. *Addit. Manuf.* **22**, 508–515 (2018).

[4] Aliheidari, N., Tripuraneni, R., Ameli, A. & Nadimpalli, S. Fracture resistance measurement of fused deposition modeling 3D printed polymers. *Polym. Test.* **60**, 94–101 (2017).

[5] Nycz, A. *et al.* Controlling substrate temperature with infrared heating to improve mechanical properties of large-scale printed parts. *Addit. Manuf.* **33**, 101068 (2020).

[6] Arbeiter, F., Spoerk, M., Wiener, J., Gosch, A. & Pinter, G. Fracture mechanical

characterization and lifetime estimation of near-homogeneous components produced by fused filament fabrication. *Polym. Test.* **66**, 105–113 (2018).

[7] McLouth, T. D., Severino, J. V., Adams, P. M., Patel, D. N. & Zaldivar, R. J. The impact of print orientation and raster pattern on fracture toughness in additively manufactured ABS. *Addit. Manuf.* **18**, 103–109 (2017).

[8] Ayatollahi, M. R. & Aliha, M. R. M. Wide range data for crack tip parameters in two disc-type specimens under mixed mode loading. *Comput. Mater. Sci.* **38**, 660–670 (2007).

[9] Nejati, M., Aminzadeh, A., Saar, M. O. & Driesner, T. Modified semi-circular bend test to determine the fracture toughness of anisotropic rocks. *Eng. Fract. Mech.* **213**, 153–171 (2019).

[10] Ayatollahi, M. R. & Aliha, M. R. M. On determination of mode II fracture toughness using semi-circular bend specimen. *Int. J. Solids Struct.* **43**, 5217–5227 (2006).

[11] Ayatollahi, M. R., Aliha, M. R. M. & Hassani, M. M. Mixed mode brittle fracture in PMMA - An experimental study using SCB specimens. *Mater. Sci. Eng. A* **417**, 348–356 (2006).

[12] Kuruppu, M. D. & Chong, K. P. Fracture toughness testing of brittle materials using semi-circular bend (SCB) specimen. *Eng. Fract. Mech.* **91**, 133–150 (2012).

[13] Lu, M., Lee, C. & Chang, F. by J-Integral Methods. **35**, 1433–1439 (1995).

[14] Duty, C. E. *et al.* Structure and mechanical behavior of Big Area Additive Manufacturing (BAAM) materials. *Rapid Prototyp. J.* **23**, 181–189 (2017).

5 Summary and future work

This report presents a study of the mechanics of FFF polymer structures with the goal of exploring processing-structure-performance relationships with respect to tensile mechanical properties and fracture behavior. The ultimate goal of qualification of FFF materials is advanced through further evaluation of the current state of the art, the processing-structure-performance relationships in uniaxial tension testing, the effects of environmental conditioning on performance, and the use of

a fracture test that allows more accurate comparison of processing conditions on the fracture toughness.

For FFF to achieve widespread acceptance in the manufacturing landscape for the production of end-user parts, testing standards specific to polymer AM must be developed, either through the adaptation of current testing standards or the creation of unique standards. Due to the inherent variability in FFF prints and the large number of possible print settings, future work needs to standardize repeatable print nomenclature, testing procedures, and specimens. This standardization should be accompanied by an integrated computational materials engineering (ICME) approach to materials qualification where multiscale physics-based modeling is used to predict the polymer chain dynamics at the interface and then adequately capture that materials response to load and quantify uncertainty from atoms to structure. Experimental and computational analysis will support the optimization of printing conditions for customized part specific requirements. The future of FFF includes embedded sensors, mid-print changes and optimizations, and expanded material systems, however the first major hurdle for FFF is the standardization of testing protocols.